Polysaccharide-Based Composite Hydrogel with Hierarchical Microstructure for Enhanced Vascularization and Skull Regeneration

Gonggong Lu,* Xiang Li, Peilei Wang, Xing Li, Yuxiang Wang, Jiayi Zhu, Alfredo Ronca, Ugo D'Amora,* Wenke Liu, and Xuhui Hui
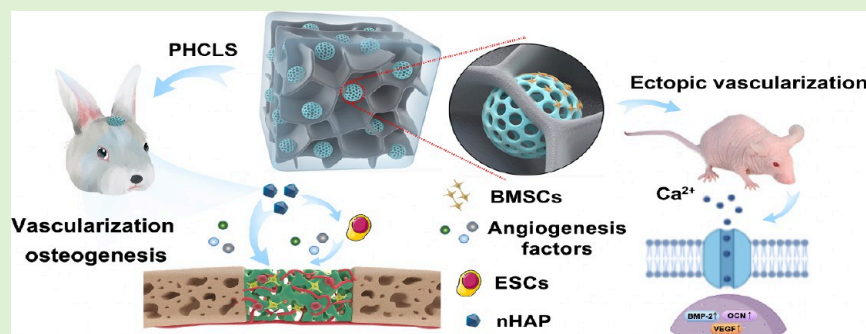
Cite This: https://doi.org/10.1021/acs.biomac.3c00655

Read Online

ACCESS | 📊 Metrics & More | 📖 Article Recommendations | 🆘 Supporting Information

ABSTRACT: Critical-size skull defects caused by trauma, infection, and tumor resection raise great demands for efficient bone substitutes. Herein, a hybrid cross-linked hierarchical microporous hydrogel scaffold (PHCLS) was successfully assembled by a multistep procedure, which involved (i) the preparation of poly(lactic-co-glycolic)/nanohydroxyapatite (PLGA-HAP) porous microspheres, (ii) embedding the spheres in a solution of dopamine-modified hyaluronic acid and collagen I (Col I) and cross-linking via dopamine polyphenols binding to (i) Col I amino groups (via Michael addition) and (ii) PLGA-HAP (via calcium ion chelation). The introduction of PLGA-HAP not only improved the diversity of pore size and pore communication inside the matrix but also greatly enhanced the compressive strength (5.24-fold, 77.5 kPa) and degradation properties to construct a more stable mechanical structure. In particular, the PHCLS (200 mg, nHAP) promoted the proliferation, infiltration, and angiogenic differentiation of bone marrow mesenchymal stem cells in vitro, as well as significant ectopic angiogenesis and mineralization with a storage modulus enhancement of 2.5-fold after 30 days. Meanwhile, the appropriate matrix microenvironment initiated angiogenesis and early osteogenesis by accelerating endogenous stem cell recruitment in situ. Together, the PHCLS allowed substantial skull reconstruction in the rabbit cranial defect model, achieving 85.2% breaking load strength and 84.5% bone volume fractions in comparison to the natural cranium, 12 weeks after implantation. Overall, this study reveals that the hierarchical microporous hydrogel scaffold provides a promising strategy for skull defect treatment.

1. INTRODUCTION

Reconstruction of large-scale skull defects due to severe trauma, tumor resection, and congenital deformity has historically been a severe problem for patients and orthopedic surgeons worldwide.[1] Bone tissue engineering (BTE) has been viewed as the ultimate solution for replacing bone grafts in the repair of skull defects. However, the long-term success of BTE is impeded by the inadequate vascularization of the engineered construct. Due to inadequate structural anastomosis of implants and a delay in early neovascularization, revascularization is currently not progressing as expected.[2] Therein, functional artificial bony implants with biomimetic structures and compositions might play an important role in the process of angiogenesis. Though exogenous cells and growth factors are key regulators of each stage for accelerating bone healing, the unpredictable clinical risk has been constraining their transformation application.[3] In the previous works, we

demonstrated that endogenous stem cells (ESCs) were successfully recruited in situ to promote early osteogenesis and quick vascularization in cell/factor-free scaffolds with improved material designs,[4–7] as well as integrating type I collagen (Col I) fibrillar matrices and hydroxyapatite (HAP) by the hybrid cross-linking mechanism mediated by dopamine-modified hyaluronic acid (HAD).[4] However, the closed pore walls and the long distance between pores in the scaffold generally restrict the cells' migration. As a result, the cells can

Scheme 1. Illustration of a Schematic for the Creation of a PHCLS Using PLGA-HAP Open Porous Microspheres and an Interconnected Hybrid Cross-Link Network Made of Multireactive Polyphenols That Serve as Links between Organic and Inorganic Components[a]
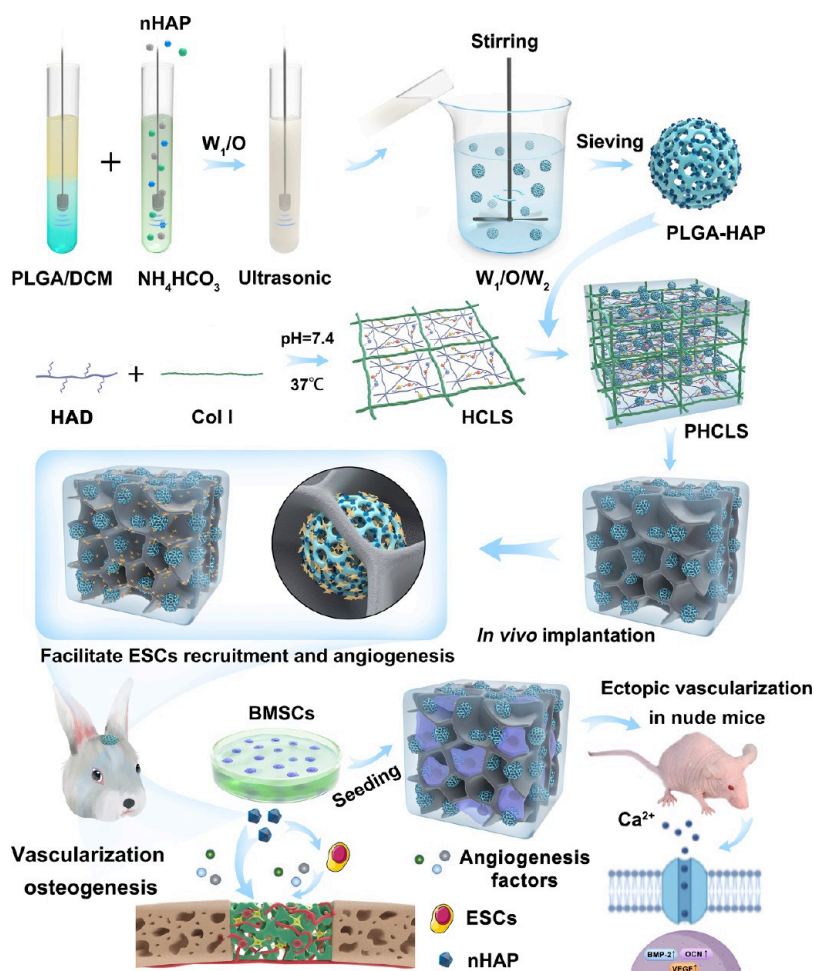
[a]The hybrid cross-linked hierarchical microporous structure within the PHCLS could not only enhance mechanical strength and structural stability of the scaffold but also promote osteogenesis by facilitating ESC recruitment and angiogenesis. Additionally, the in vivo investigation revealed that the PHCLS might speed up bone repair following implantation into the critical-sized skull defect model in rabbits and the subcutaneous model of mice.

only adhere to and multiply on a single pore, severely restricting their ability to migrate and multiply and precluding the use of scaffolds to promote neovascularization. Therefore, optimizing the pore communication and the diversity of pore sizes of the scaffold is crucial for promoting oxygen (O_2) and nutrient transport as well as cell migration, which might benefit blood transport connections and accelerate skull regeneration.

Generally, hydrogel scaffolds contain only pores with a relatively single pore size. Inspired by the remarkable property of natural bone, three-dimensional (3D) hierarchical microporous scaffolds are interspersed with interconnected small pores between large pores, which can penetrate the closed pore walls, provide transportation "highways" on various scales during osteoregeneration, and promote the growth, development, and maturation of blood vessels.[8,9] Numerous studies have concluded that interconnected microporosity with a diameter smaller than 100 μm imparts biomimetic characteristics to the scaffold and improves its biological activity due to the increased specific surface area of ion-exchange phenomena in contact with biological fluids.[10,11] In addition, micropores (100−500 μm) are essential for allowing the bone to develop

and vascularize as well as for lowering Young's modulus, which lowers the danger of stress shielding and reduces stiffness mismatches with natural tissue (despite the decreased mechanical strength of scaffolds).[12] In addition, cell attachment, biomineralization, and osteointegration in vivo are significantly influenced by the microtopology of the material's surface.[13,14] Based on prior studies, we think that the incorporation of hierarchical microporous structures into hydrogel scaffolds will unavoidably become a trend in order to attain the best vascularization and osteogenic qualities.

Synthetic polymers are of interest because they allow the relatively simple fabrication of scaffolds with open microporous structures and adapted mechanical properties and degradation rates.[15] Poly(lactic-co-glycolic) acid (PLGA) is one of the common biodegradable polymers to produce bone scaffolds[16,17] and was approved by the US Food and Drug Administration for clinical use. In addition, PLGA is a linear copolymer with varying ratios of its monomers GA (glycolic acid) and LA (lactic acid), which offers a wide range of degradation rates[18] that can be tailored to specific needs. Despite these advantages, its weak "osteoconductivity" or

constrained "osteoinductivity" leads to unfavorable therapeutic effectiveness.[19] As a result, the creation of composite open-porous PLGA scaffolds combined with nano-HAP (nHAP) (referred to as PLGA-HAP) may result in improved osteoconductivity and sufficient mechanical characteristics to sustain the load of the growing tissue throughout the regeneration process, as previously proven.[20,21] Additionally, it has been demonstrated that nHAP controls the pore size and porosity of PLGA porous microspheres and increases surface roughness, positively affecting the adhesion and migration of extracellular matrix (ECM) proteins to the scaffold and thereby promoting cell adhesion, migration, and osteoblast differentiation.[22]

Our earlier research has demonstrated that adding polyphenols, like dopamine (DA), may control how Col I, HA, and HAP's hybrid cross-links are integrated at the interface.[4,6] DA has long been regarded as a crucial adhesion functional group.[23] The catechol group and lysine residues are present in DA, a substance that is prevalent in both plants and animals, and it has the same outstanding adhesion properties as -3,4-dihydroxyphenylalanine (DOPA), which is found in naturally occurring mussels.[24] Additionally, DA can oxidize and self-polymerize into polydopamine (PDA) when dissolved in alkaline aqueous solutions under aerobic circumstances.[25] PDA can successfully facilitate cell attachment and proliferation on the surface of bone tissue-manufactured scaffolds due to its superior adhesion and chemical reactivity. Additionally, PDA alteration can promote the enrichment of calcium ions (Ca^{2+}) on the surface of bone healing materials, giving apatite nucleation sites and aiding in their production. This is because PDA contains a large number of catechol groups, which have a strong chelating effect on Ca^{2+}. Last but not least, PDA functionalization may be an appropriate strategy to improve the hydrophilic properties of bone healing materials. For instance, Yang and co-workers lowered the contact angle when they changed poly -lactic acid (PLLA) nanofibers with PDA coating.[26] Recently, DA has been used to functionalize natural polymers such as gelatin or HA,[4,27,28] and the results showed that the scaffolds promoted osteogenic differentiation of bone marrow mesenchymal stem cells (BMSCs) and upregulated the expression of osteogenic-related proteins. Indeed, in vivo results in a cranial defect model in rabbits and beagle dogs showed that the scaffold was able to stimulate cranial bone repair by accelerating osteogenic differentiation and launching angiogenesis.[4]

Herein, we designed a 3D dopamine-mediated hierarchical microporous scaffold that combined open microporous spheres based on PLGA-HAP with interconnected perfusable macro-channel networks constructed by HAD cross-linking Col I, which may further provide hierarchical porous space to enhance vascularization and enhance bone regrowth. According to Scheme 1, we first fabricated PLGA-HAP with different pore sizes and porosity through a two-phase emulsification technique (water-in-oil-in-water, W_1-O-W_2) by regulating HAP content. Subsequently, the PLGA-HAP porous microspheres were embedded into the hydrogel matrix, while dopamine-mediated hydrogels were used to create the hierarchical microporous scaffolds (PHCLSs) with the structure of the interwoven hybrid cross-link network functioning as links between organic and inorganic components, multireactive polyphenols linked to amino groups of Col I by Michael addition reactions and to PLGA-HAP through Ca^{2+} chelation. The hierarchical microporous structure within

the PHCLS may not only enhance nutrient transportation but also improve mechanical strength and structural stability. Proliferation, migration, and differentiation of BMSCs as well as the ability to recruit ESCs were examined using in vitro cellular tests and a rabbit model of cranial defects. Moreover, PHCLSs were subcutaneously implanted into a mouse model and a critical-sized skull defect model in rabbits, to assess in vivo the ectopic angiogenesis and osteogenesis of scaffolds and long-term bone regeneration, respectively.

2. MATERIALS AND METHODS

2.1. Materials. PLGA [LA:GA = 50:50, M_w (molecular weight) = 110 kDa] was purchased from Evonik Ind. The National Engineering Research Center for Biomaterials, Sichuan University, Chengdu, China, provided the nHAp slurry. Bloomage Freda Biopharma Corporation (Shandong, China) supplied HA (cosmetic grade, M_w = 0.34 MDa), Trauer company (Guangzhou, China) supplied Col I, and Best Reagent Corporation (Chengdu, China) supplied N-hydroxysuccinimide (NHS, 99%) and DOPA hydrochloride (DOPA·HCl). Dichloromethane (DCM), ammonium bicarbonate (NH_4HCO_3), poly(vinyl alcohol) (PVA), ethanol, acetic acid, sodium hydroxide (NaOH), hydrogen peroxide (H_2O_2), and phosphate buffered saline (PBS) were purchased from Chengdu Kelong Chemical Technology Co., Ltd., China. Hyclone, USA, provided the α-Minimum Essential Medium (α-MEM), fetal bovine serum (FBS), and penicillin/streptomycin (PS). Triton X-100, rhodamine-phalloidin, 4′,6-diamidino-2-phenylindole (DAPI), hyaluronidase, and collagenase were acquired from Sigma-Aldrich, USA. Fluorescein diacetate (FDA), propidium iodide (PI), paraformaldehyde, gluta-raldehyde, and PI were also purchased.

2.2. Fabrication of PLGA-HAP Open Porous Microspheres. PLGA-HAP open porous microspheres were fabricated by the double emulsion evaporation method.[29] Briefly, 300 mg of PLGA was dissolved in 6 mL of DCM and then 2 mL of NH_4HCO_3 (1.25 g/50 mL) was added to the PLGA/DCM mixture by a syringe. To form open porous PLGA-HAP microspheres, with different pore sizes and porosities (PLGA, $PLGA-HAP_1$, and $PLGA-HAP_2$), nHAP slurry (0, 1, and 2 mL; 200 mg/mL) was added into the PLGA/DCM mixture. After ultrasonic emulsification for 15 min under ice bath conditions, the emulsion was added dropwise to 25 mL of PVA (1% w/v) solution to form a W_1-O-W_2 double emulsion. Then, the mixture was centrifugally stirred at 1200 rpm/min for 15 min at room temperature. After this, 50 mL of deionized water (DDW) was added and stirred overnight. To ensure complete evaporation of DCM, the sample was centrifugally cleaned repeatedly with DDW and vacuum freeze-dried.

2.3. Preparation of HAD. HAD was synthesized as previously reported in our work.[4] One millimolar HA was dissolved in 35 mL of 0.01 M PBS. Following this, EDCI (960 mg, 5 mM) and NHS (230 mg, 2 mM) were dissolved in the solution. To activate the carboxyl group on HA, the process was run for 2 h at a pH of 4.75−5.0. The combination was then treated with 2 mmol of DOPA·HCl and allowed to react for 12 h at a pH of 5. The complete process was carried out in an oxygen-free environment. Following the reaction, the solution was dialyzed against acidic DDW (pH 3.5) at room temperature for 72 h, with the water being replaced periodically. HAD as a solid was obtained by freeze-drying the dialysate. HAD's molecular structure was determined by nuclear magnetic resonance ^1H NMR (400 MHz, Bruker AMX-400, USA). ChemNMR was used to assess the grafting ratio of dopamine.

2.4. Construction of the PHCLS. First, the HAD and Col I solution were prepared. 25 mg of HAD was weighed and vortex oscillation-solubilized in 1 mL of DDW thoroughly. Prelyophilized Col I was similarly dissolved in a 0.5 M acetic acid solution at 4 °C at a concentration of 25 mg/mL. PLGA-HAP was first mixed with HAD solution under sonication for 5 min, and the final weight ratio of the microspheres was controlled as 50% of the total polymer mass. After which, two groups of liquid were immediately injected into a silicone

mold with dimensions of 8 mm in diameter and 3 mm in height and exposed to air at a temperature of 37 °C for 10 min. The two groups of liquids were then pH-adjusted to 7.4 by adding a NaOH (2 M) solution. After freeze-drying, the hydrogel was maintained at ambient temperature for 24 h to allow for optimal cross-linking among the various components, and three groups of hierarchically microporous scaffolds (P₁HCLS, P₂HCLS, and P₃HCLS) and HCLS, used as control, were obtained based on PLGA-HAP containing different nHAP amounts (0, 1, and 2 mL; 200 mg/mL, respectively) (Table 1).

Table 1. Nomenclature and Chemical Composition of PLGA-HAP Open Porous Microspheres in the Different PHCLS

scaffold nomenclature	nHAP content
HCLS	
P₁HCLS	0
P₂HCLS	200 mg
P₃HCLS	400 mg

2.5. Characterization of nHAP, PLGA-HAP Microspheres, and PHCLSs. The particle size of nHAP was investigated by a nanolaser particle size analyzer (ZEN3690, Malvern) and transmission electron microscopy (TEM, JEOL, JEM-2100Plus, Japan) and scanning electron microscopy (SEM, Hitachi, S-4800, Japan) were used to investigate the micro- and nanostructure. The crystalline phases of nHAP were determined using an X-ray diffractometer (XRD; Empyrean, PANalytical B.V.) at a scanning rate of 0.02°/s in a 2θ range from 5° to 80° with Cu Kα radiation (λ = 0. 154056 nm). The mean microsphere diameter and size distribution of the PLGA-HAP microspheres were characterized by using a Coulter LS230 laser particle size analyzer (Beckman, UK). The component of nHAP in PLGA-HAP was quantitatively analyzed by using a thermogravimetric analyzer (Diamond TG/DTA; PerkinElmer Instruments). Briefly, 3–6 mg of PLGA-HAP microsphere powder with different nHAP concentrations was weighed and the temperature range was from 25 to 1000 °C and the heating rate was 20 °C/min. The structural morphology of the PLGA-HAP and PHCLS were examined by SEM and the ratio and distribution of calcium and phosphorus of PLGA-HAP were characterized by electronic energy spectroscopy (EDS). ImageJ was used to semiquantify pore size and porosity according to the SEM images. AFM (Dimension ICON, Bruker, Germany) in tapping mode at ambient circumstances with a resonance frequency of 75 kHz was used to evaluate the surface nanotopography and roughness of the scaffolds. The test results for the root-mean-square (RMS) were determined by averaging the values obtained from four nonoverlapping sample locations (15 by 15 μm). The PLGA-HAP pore diameter and porosity were determined by using a mercury porosimeter (PoreMaster-33GT, USA). A stereo microscope (SYCOP 3, ZEISS) was used to characterize the general appearance of PLGA-HAP and the PHCLS at various shooting magnifications. nHAP was labeled with calcein (10 μM/mL), which can specifically bind with nHAP for 20 min at room temperature,[30] and gently rinsed with DDW five times. The scaffolds were placed in an incubator at 37 °C for 7 days, and the simulated body fluid (SBF) was refreshed every 24 h to maintain a consistent ionic strength throughout the experiment.

The compressive storage (G') and loss moduli (G'') were mechanically characterized using a dynamic mechanical analyzer (DMA, TA-Q800, USA) in multifrequency mode at a prestressed force of 5 mN, amplitude of 20 μm, and fixed frequency of 1–10 Hz in constant room temperature. A cylindrical hydrogel sample of 5 mm in height and 8 mm in diameter was placed on the DMA platform for the static compression mechanical test, and each sample was tested three times. The hydrogel was then crushed until it fractured at a rate of 2 N/min. The mentioned method was also used to determine the scaffolds' mesh size (ζ),[31] based on the following equation:

$$\zeta = [(G'N_A)/RT]^{-1/3}$$

G' stands for the storage modulus, whereas N_A and R stand for the molar gas constant and temperature, respectively.

For the structural stability test of the PHCLS, the swelling behavior of different scaffolds was analyzed. Briefly, the disk-shaped scaffolds were prepared by the method described above. Thereafter, the scaffolds were washed in DDW, freeze-dried, and weighed (W_d). Then, the freeze-dried scaffold was immersed into 10 mL of PBS buffer (pH 7.4) and placed in a shaker (ZHWY-2012C, Shanghai Zhicheng, China; 90 rpm, 37 °C). In order to establish inflated equilibrium, the scaffolds were finally weighted (W_s) at predetermined intervals. Three replicates of each sample's measurement were performed. The formula shown below was used to determine the scaffold's swelling rate:

$$\text{Swelling ratio} = (W_s - W_d)/W_d \times 100\%$$

The degradation behavior of nHAP was evaluated by detecting Ca^{2+} release from microspheres. Ten milligrams of microspheres were first impregnated in a glass vial containing 4 mL of calcium-free PBS and placed in a shaker (75 rpm, 37 °C). All release media were collected at the predetermined time point and 4 mL of fresh PBS was added. Atomic absorption spectroscopy (PinAAcle 900T, PerkinElmer, USA) was used to detect Ca^{2+} release concentrations at 422.7 nm (n = 3). The standard curve of concentration and absorption values was established in advance, and the concentration gradients of Ca^{2+} standard solution were 3, 1.5, 0.75, 0.375, 0.1875, and 0.09375 μg/mL.

The disintegration performance was tested. The prepared disk-shaped scaffolds were washed, freeze-dried, and weighed (W_o). The scaffolds were then submerged in 10 mL of PBS that contained 100 U of either type I collagenase or hyaluronidase, and they were shaken at 90 rpm at 37 °C to maintain the constant temperature. The scaffolds were then removed, cleaned in DDW, dried by freezing, and weighed once more (W_r). Three duplicate measurements were made for each sample. The disintegration behavior was estimated as follows and reported as a percentage of weight retention:

$$\text{Weight retention percentage} = (W_o - W_r)/W_o \times 100\%$$

2.6. Cell Proliferation and Differentiation In Vitro. From the bone marrow of newborn rabbits, BMSCs were taken out and grown to passage 3. A 20 μL solution of 1×10^6 mL^{-1} BMSCs was applied to the scaffold surface and allowed to permeate in order to create a scaffold-cell cocultured complex. In an ultralow attachment 24-well plate (Costar, USA), the complex was grown in α-MEM containing 10% FBS and 1% PS. The medium was replaced every 48 h and each well held 2 mL of it. After coculturing for 3, 7, and 14 days, the CCK-8 test was carried out to assess the scaffolds' biocompatibility. Each well received 150 μL of media containing 10% CCK-8, which was then added, and the complex was allowed to incubate there for 3 h. Cell density was then determined by measuring the OD at 450 nm. Additionally, using confocal laser scanning microscopy (CLSM, LSM 880, ZEISS), live/dead labeling of BMSCs was seen after cells were stained with 1 μg/mL of FDA and PI. CLSM was used to examine the cytoskeletons of the BMSCs in the complexes. The scaffolds were stained for 3 h with rhodamine-phalloidin (5 μg/mL) and for 1 min with DAPI (10 μg/mL) after being fixed for 25 min with 4% paraformaldehyde and transparentized for 10 min with 0.1% Triton X-100. To investigate the spreading morphology of BMSCs on the scaffolds, samples were fixed with 2.5% glutaraldehyde solution for 48 h at 4 °C, dehydrated with gradient ethanol, and dried with critical point drying for 1.5 h.

After different days of coculturing, the relative expression levels of genes linked to angiogenesis and osteogenesis were examined using real-time quantitative PCR (RT-PCR). The RNeasy Mini Kit (Qiagen) was used to extract the total RNA from the BMSCs growing on the scaffolds, and a NanoDrop 2000 spectrophotometer (Thermo Scientific, USA) was used to measure the amount of RNA present. The iScript cDNA Synthesis Kit (Bio-Rad) was then used to convert RNA into cDNA. SYBR Green Supermix (Roche, USA) was used for quantitative RT-PCR on a CFX96 RT-PCR detection system

from Bio-Rad. The relative gene expression levels were estimated using the $2^{-\Delta\Delta Ct}$ technique using GAPDH as an internal reference. Supporting Information Table S1 lists the primers that were used to evaluate the expression levels of BMP-2, osteocalcin (OCN), and vascular endothelial growth factor (VEGF). Based on GAPDH's level of gene expression, all other genes' expressions were computed. The scaffolds were paraffin-embedded and sectioned after being fixed with 4% paraformaldehyde. To further assess BMSC migration and angiogenic differentiation, immunofluorescence (IF) labeling on CD44 and CD31 was done. Slices were subjected to citric acid antigen retrieval solution for 1 h prior to being incubated for 1 h at 37 °C with primary antibodies (mouse anti-rabbit, NB600-450, NOVUS, 1:200) for IF labeling. Following the addition of the autofluorescence quencher, BSA was incubated for 30 min. The primary antibody was then pipetted onto the sections and allowed to sit there for 12 h at 4 °C. The samples were then treated for an additional hour with the secondary antibody (Goat anti-Rabbit IgG(H+L) FITC-conjugated, Thermo Fisher Scientific, G-21234, 1:100), followed by PBS washings. After DAPI restaining the nucleus, the sections were sealed with antifluorescence quenching tablets for observation. In addition, immunohistochemical (IHC) staining of alkaline phosphatase (ALP) and Alizarin Red staining (ARS) were used to characterize the osteogenic proteins and calcium deposition in vitro. Primary mouse anti-rabbit antibodies (Abcam, ab224335, 1:150) were utilized for IHC with ALP. Proteinase K (20 mg/mL, pH 7.4) was used to extract antigens from the sections by heating them to 25 °C for 15 min. Later, nonspecific binding was blocked for 4 h using 10% goat normal serum. The slices were then treated at 4° for 12 h with primary antibodies. The sections were then treated with the mouse specific HRP-DAB (ABC) detection kit (PV-9002, ZSGB-BIO) for color development and counterstained with hematoxylin following a 15 min period of inhibiting endogenous peroxidase with 3% H_2O_2. For ARS staining, the sections were dyed with Alizarin Red dye solution (Beyotime, C0138) for 5 min and then the dye solution was removed, washed twice with PBS, dried, and sealed for observation.

2.7. Ectopic Angiogenesis and Osteogenesis in the Subcutaneous Implantation Model. Using a subcutaneous implantation approach in naked mice, the ectopic angiogenesis and osteogenesis of scaffolds were assessed.[4] The Sichuan University Medical Ethics Committee gave its approval to all animal experiments, and all methods followed the university's policies regarding the handling and use of lab animals. BMSCs were seeded at a density of 2 × 10^5 cells per scaffold onto the surface (d = 8 mm; h = 2 mm). Pentobarbital sodium was injected intraperitoneally to anesthetize naked mice before BMSC-laden scaffolds were subcutaneously implanted into the naked mice. The naked mice were put to death after 4 weeks, and the explants' diameters were then measured. Prior to and following implantation, the storage modulus of scaffolds was evaluated by DMA. For the purpose of quantifying BV/TV and BMD at 15 μm volume pixel and visualizing the impact of mineral deposition, microcomputed tomography (Micro-CT, Viva CT80, Scanco Medical AG) was used. The 3D image of the mineralized scaffolds was recreated using the mimics program (Materialize). The microstructure of the scaffolds and in vivo-mineralized hydroxyapatite deposition was observed by SEM, and calcium/phosphorus element mapping was used to pinpoint mineral deposition. The scaffolds were then stained with rhodamine-phalloidin/DAPI, examined by CLSM, and ImageJ was used to semiquantify the number of cells. The samples underwent the aforementioned processing steps for paraffin sectioning, hematoxylin and eosin (H&E), ARS, IF, and IHC staining (CD31, BMP-2, and VEGF). For H&E staining, sections were treated with hematoxylin for 5 min, then differentiated with hydrochloric acid solution, and returned to blue with ammonia solution. After dehydration with gradient alcohol, the samples were stained with eosin solution for 5 min and sealed with neutral gum. The IHC staining procedure of VEGF (Abcam, ab32152, 1:200) was similar to that described above. Using ImageJ software, the semiquantitative average optical density (AOD value) findings for IF and IHC stainings were calculated.

2.8. Vascularization and Bone Regeneration Assessment in the Critical-Sized Rabbit Calvarial Bone Defect Model. The recruitment capacity of ESCs and long-term bone repair were assessed using a rabbit skull defect model (Φ = 10 mm).[6] Six adult New Zealand white rabbits (2.5−3.0 kg, male, 2.5−3 months old, n = 3) were implanted with all four groups. The Sichuan University Medical Ethics Committee (KS2022903) authorized all animal trials. All animal treatments were carried out in compliance with Sichuan University's Guidelines for the Care and Use of Laboratory Animals. After being sedated with 20 mg/mL pentobarbital sodium, scaffolds were implanted into the cranial bone defects on each side. The implants were removed after a week, fixed in 4% paraformaldehyde, embedded in paraffin wax, and cut into sections with a thickness of 5 μm for H&E, IHC, and IF staining. By using ImageJ software, the mean fluorescence intensity of the IF staining was semiquantified. In order to evaluate the morphology of ESCs using SEM, samples were immobilized with 2.5% glutaraldehyde, dehydrated with gradient ethanol, and sprayed with gold.

For the in vivo study, 48 male New Zealand white rabbits weighing 2.5−3 kg and 2.5 to 3 months old were chosen. The rabbits without any surgery were classified as the natural group, while the deformed area without any filler was assigned as the blank group. On the basis of whole blood obtained at weeks 4 and 12, the levels of the inflammatory cytokines IL-6, IL-1β, and tumor necrosis factor alpha (TNF-α) were measured using enzyme-linked immunosorbent assay kits. After 4 and 12 weeks following surgery, euthanasia was carried out. The integration of the scaffold with the surrounding cranium was examined using a push-out model, and samples at the faulty site were pushed out using mechanical testing equipment (Shimadzu, EZ-LX 1 kN, Japan). By using a digital X-ray device with an exposure time of 1.8 s at 62 kVP and 250 mA, all samples were radiographed. The rabbit craniums were collected, fixed for 14 days in 4% paraformaldehyde, and scanned using micro-CT. CTvox software was used to import the obtained data for display and analysis. Using CTAn software, the BV/TV, BMD, and other parameters of the targeted region were also computed for each sample. The samples underwent a 2 month decalcification process in 10% ethyl-enediaminetetraacetic acid solution, followed by a gradient alcohol dehydration step, paraffin embedding, and sectioning for H&E, Masson's trichrome (MT), IF, and IHC staining. For MT staining, the slices were sequentially soaked in potassium bichromate overnight and then impregnated with iron hematoxylin for 3 min. Then, they were immersed in Lichun acid fuchsin and phosphomolybdate solution for 10 and 3 min, respectively, and finally stained with aniline blue solution for 6 min. Protease/phosphatase inhibitor (Thermo Fisher Scientific) and RIPA buffer (Beyotime) were used to capture the total proteins from tissue homogenates. Following electrophoresis on 10% SDS-polyacrylamide gel, it was transferred to polyvinylidene difluoride membranes and then blocked in 5% nonfat milk. Membranes were washed three times in TBS with 0.1% Tween-20 following the overnight incubation at 4° with primary antibodies (Runx2, Abcam, ab23981, 1:1000; BMP-2, Abcam, ab284387, 1:1000; OCN, GENETEX, GTX13418, 1:600; and VEGF, Abcam, ab32152, 1:1000). Following a 1 h incubation period with secondary antibodies (Goat anti-Mouse IgG (H+L) HRP, Invitrogen 31430, 1:5000), washing in TBS containing 0.1% Tween-20 and imaging were performed.

2.9. Statistical Analysis. The averages and standard deviations of three typical experiments were used to express all data. GraphPad Prism software (GraphPad Software Inc.) was used to analyze the data. Student's t-test (unpaired and two-tailed), one-way or two-way ANOVA, and the Tukey post hoc test were all used. At $p < 0.05$, the values were deemed to be statistically different.

3. RESULTS AND DISCUSSION

3.1. Characterization of Open Porous Microspheres. Bone is a natural composite material composed primarily of type I collagen (an organic polymer) and HAP (an inorganic mineral phase).[32] The skull, which is characterized by the
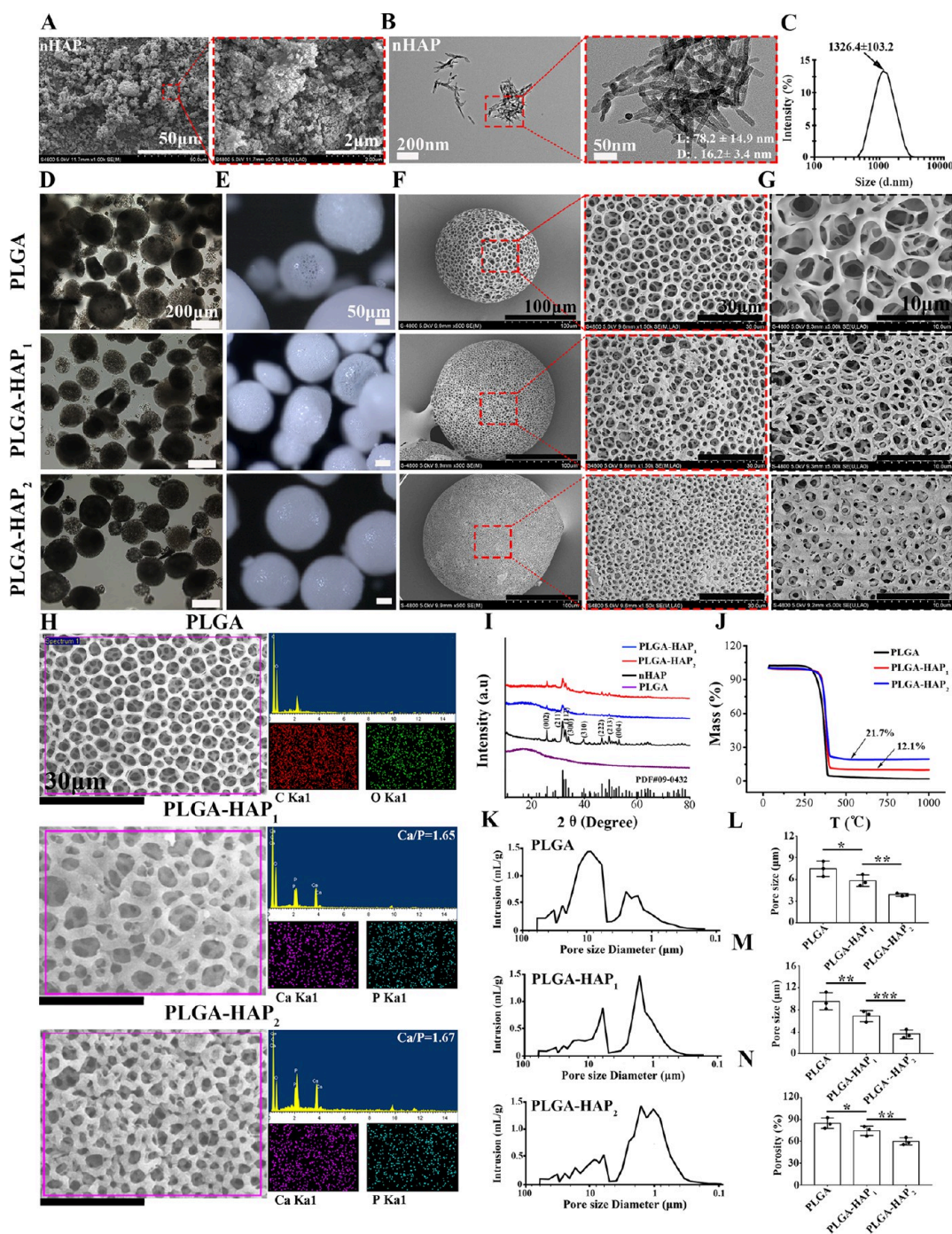
Figure 1. Characterization of nHAP and PLGA-HAP open porous microspheres. (A) Representative SEM images and (B) TEM images of nHAP. (C) Size distribution of nHAP measured by DLS. (D) Representative microscopy images and (E) stereomicroscopy images of the porous microspheres. (F) SEM images of open porous microspheres in the surface and (G) cross-sections. (H) EDS mapping images of different microspheres. (I) nHAP's typical spectrum and the X-ray diffraction spectra of a variety of microspheres. (J) TGA analysis of specimens. (K) Characterization of pore size distribution of different microspheres based on the mercury injection method. (L) Pore size of the surface and (M) cross-section of diverse microspheres. (N) Porosity of different microspheres based on the mercury injection method. PLGA-HAPi denotes the porous microspheres. The letter "*i*", with *i* = 1 or 2 denotes the intermediate and high nHAP amount, respectively. *n* = 3 independent experiments per group; the significance levels were established at $p < 0.05$ (*), $p < 0.01$ (**), and $p < 0.001$ (***), respectively.

presence of the trabecular or spongy bone, is a highly porous structure with a cross-section that resembles a honeycomb material. In the meantime, it has extensive blood vessels and frequently has red bone marrow, which is where blood cells are made. One major obstacle to the regeneration of the skull is the challenge of providing adequate vascularization to bone substitutes for oxygenation of newly generated tissues. Only

diffusion between 150 and 200 μm from the supplying blood arteries can provide the amount of oxygen necessary for cell survival[33]; thus, angiogenesis plays a critical role in the success of skull reconstruction. Here, we created a 3D hierarchical microporous scaffold mediated by polyphenols, which mimics the structural and chemical characteristics of the skull and encourages host vascularization. The osteoconductive bimodal

macro/microporous structure, mechanically adjustable capabilities, and degradation rate to enable bone formation are the distinguishing characteristics of this hierarchical microporous scaffold. These interconnected macro/micropores provided tissue ingrowth and nutrient transportation "highways" on various scales during osteoregeneration while preserving crucial pore size throughout the hydrogel phase. The major methodology for creating 3D ordered hydrogel scaffolds with highly linked macropores is 3D printing. Currently, porous hydrogel scaffolds typically only comprise relatively single pore size.[34−36] Although the fabrication of hierarchical microporous hydrogel scaffolds using 3D printing is accurate and precise, the inherent imprintability of the matrix necessitates the use of printable ink for molding, which significantly reduces the success of the hierarchical microstructure and biological properties of the hydrogel scaffolds.

To solve this problem and to construct a scaffold with hierarchical micropores, adequate mechanical strength, and a suitable degradation rate to support in vivo bone regeneration, a "pore size/porosity controlling" and "hybrid cross-link reinforcing" method was developed by open porous microspheres (PLGA-HAP) interleaving polyphenol-mediated hydrogel scaffolds. As illustrated in Figure 1, PLGA-HAP was fabricated using a W_1-O-W_2 process, as described in Section 2.2. Microspheres with porosity were generated using NH_4HCO_3 in the internal aqueous phase during the fabrication process, and pore diameters were regulated through treatment with different contents of nHAP (PLGA, PLGA-HAP_1, and PLGA-HAP_2), which affected the surface tension in the liquid phase. The morphology of nHAP was determined using SEM and TEM. Figure 1A,B shows a needle-shaped structure of nHAP with an average length of 78.2 ± 14.9 nm and granularity of 16.2 ± 3.4 nm, which imparted biomimetic features to PLGA-HAP, as the surface roughness provided by the acicular structure could enhance cell adhesion to the surface. The particle size quantified by DLS (Figure 1C) revealed a good dispersion of nHAP in water, and the average particle size was 472.4 ± 13.1 nm. Due to the open porous structure, all three kinds of microspheres showed good light transmission under an optical microscope, while the light transmittance decreased with an increase in nHAP content (Figure 1D). The porous morphology of the microspheres was further verified by a stereomicroscope, and the surface of PLGA-HAP_2 was obviously more compact as compared to PLGA (Figure 1E). Highly open porous and interconnected superficial structures were observed in the SEM images (Figure 1F) and there was a significantly decreased averaged pore size (PLGA: 7.3 ± 1.1; PLGA-HAP_2: 3.8 ± 0.4 μm) compared to nontreated microspheres (Figure 1L). Interestingly, the complete open porous structure was also achieved inside the microspheres, while treating the microspheres with higher contents of nHAP resulted in signs of aperture reduction (PLGA: 8.8 ± 0.9; PLGA-HAP_2: 2.9 ± 1.1 μm) and hole wall thickening of the microspheres (Figure 1G,M). EDS mapping confirmed the presence of a uniform distribution of calcium/phosphorus elements on both PLGA-HAP_1 and PLGA-HAP_2, and the ratio of calcium to phosphorus was in agreement with that of nHAP (Figure 1H).

In accordance with nHAP's standard card (PDF#09-0432), XRD (Figure 1I) results showed that PLGA-HAP_1 and PLGA-HAP_2 still had strong diffraction peak intensities in the (211), (002), and (300) crystal planes, proving that nHAP was successfully integrated to PLGA while the combination did not damage nHAP's physical phase structure. TGA results showed that the content of nHAP in the PLGA-HAP_1 and PLGA-HAP_2 groups was 21.7% w/w and 12.1% w/w, respectively, and there was no additional weight loss phase (Figure 1J). To further characterize the pore size and porosity of various microspheres, the mercury injection method was used, and the results showed that the pore size distribution was different for each group due to diverse contents of nHAP treatment. The average pore diameter of PLGA was 8.9 ± 1.6 μm, and the parameters of the treated groups were 6.5 ± 0.8 and 4.1 ± 0.7 μm for PLGA-HAP_1 and PLGA-HAP_2, respectively, which was in accordance with the SEM results (Figure 1K). Compared with the porosity of the PLGA group ($87.9 \pm 8.3\%$), there was a relative decrease in PLGA-HAP_1 ($73.1.9 \pm 6.8\%$) and PLGA-HAP_2 ($60.5 \pm 7.2\%$) groups, suggesting that the introduction of nHAP could achieve certain regulation on the pore structure of PLGA-HAP (Figure 1N).

The morphologies of the three groups of microspheres were further analyzed by SEM and AFM. As shown in Figure S1A, high-magnification SEM images revealed that compared with the smooth porous morphology of the PLGA surface, the micropores on the PLGA-HAP_1 and PLGA-HAP_2 surfaces were covered by evenly dispersed nHAP, which could improve the surface roughness of both to a certain extent. AFM was used to better visualize the surface nanotopography of the PLGA-HAP microspheres. PLGA-HAP_1 had higher surface roughness (RMS: 846.1 ± 57.4 nm) as compared to the other groups (PLGA: RMS = 376.3 ± 76.5 nm; PLGA-HAP_2: RMS = 504.2 ± 68.7 nm) (Figure S1B), which was consistent with the SEM results.

In summary, the use of NH_4HCO_3 and nHAP in the internal aqueous phase synergistically generated open porous microspheres with controllable interconnected micropores ($2.9-8.8$ μm) and porosity ($60.5-87.9\%$), while nHAP was evenly distributed in PLGA-HAP_1 and PLGA-HAP_2. This could be attributed to the carbon dioxide (CO_2) released by NH_4HCO_3, leading to pore opening while the higher content of nHAP increases the viscosity of the aqueous phase, resulting in the increase of surface tension and the decrease of pore size. Since the surface roughness generated by relatively small pores can improve cell adherence to the substrate, the controlled micropore structure gave PLGA-HAP biomimetic characteristics.

3.2. Characterization of the Hierarchical Microporous Hydrogel Scaffold.
Our previous study proved that the introduction of polyphenols, such as DA,[4−7] could induce angiogenesis and through the catechol-mediated Michael addition reaction and Ca^{2+} chelation, HAD might operate as a macromolecular cross-linking agent to improve the integration of the nanointerface between Col I and nHAP. Since Ca^{2+} plays a pivotal role in modulating osteoblastogenesis, Ca^{2+} release characteristics of P_2HCLS and P_3HCLS were further analyzed. As shown in Figure S2, Ca^{2+} release from the two groups of microspheres was relatively similar during the time period of $1-5$ days. However, the Ca^{2+} release of P_3HCLS was higher than that of P_2HCLS in the $7-12$ day range, which was due to the high nHAP content in P_3HCLS and the easy water absorption and release of Ca^{2+}. On the whole, the Ca^{2+} release characteristics of P_2HCLS and P_3HCLS are similar, and the amount of Ca^{2+} release is higher in the late stage. Based on previous reports and our results, the hierarchical microporous scaffold (P_1HCLS, P_2HCLS, and P_3HCLS) was prepared through a hybrid cross-linking reaction
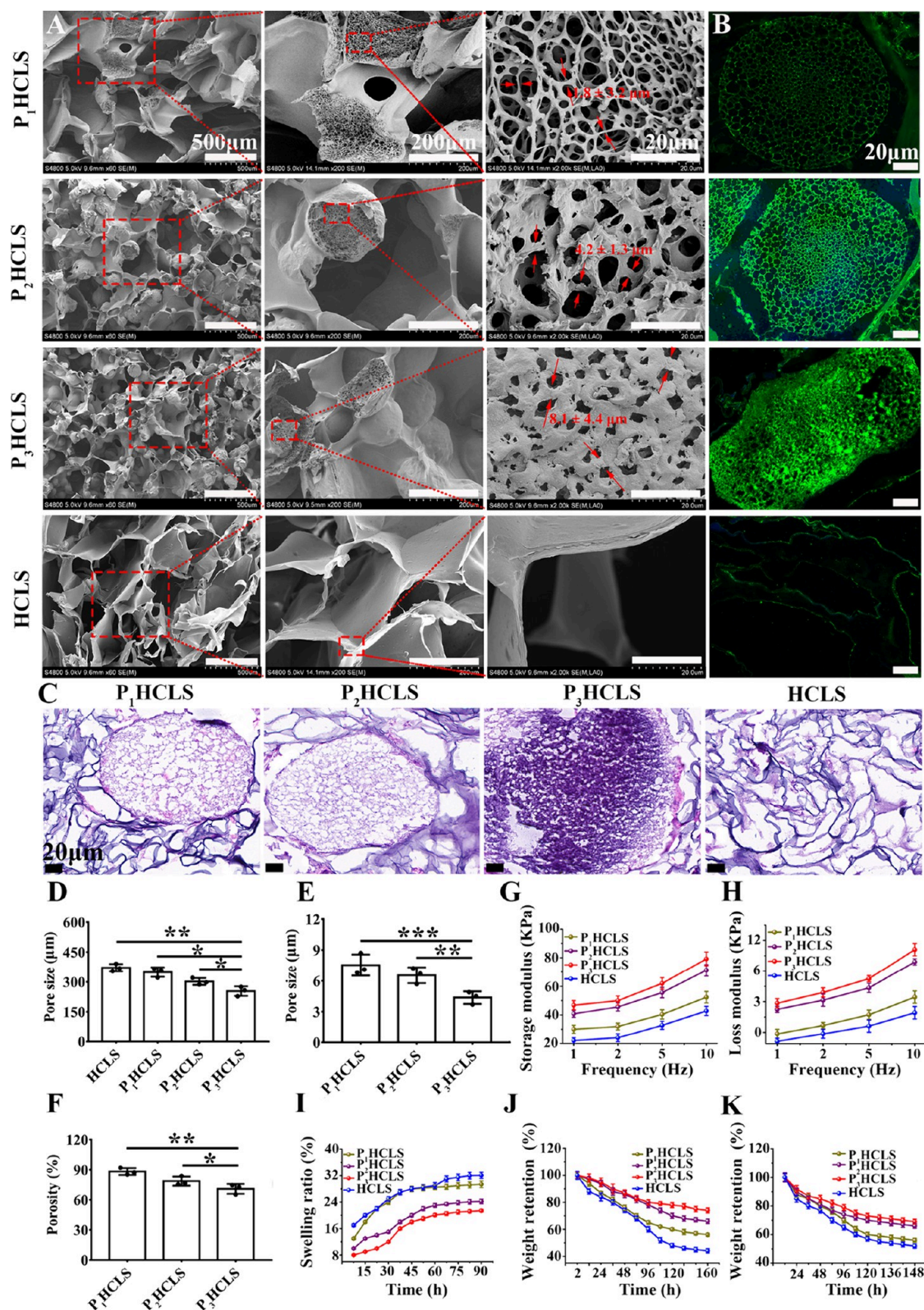
Figure 2. Characterization of the hierarchical microporous hydrogel scaffolds. (A) Representative SEM images of the hierarchical microporous structure. (B) Calcein staining of sample sections observed by CLSM. (C) H&E staining of sample sections observed by an optical microscope. (D) Semiquantitative analysis of the macropore size in various scaffolds based on SEM images and ImageJ software. (E) Micropore size in different scaffolds. (F) Porosity of different scaffolds semiquantitatively analyzed based on SEM images and ImageJ software. (G) Storage and (H) loss moduli of scaffolds. (I) Swelling ratio of various scaffolds. (J) Disintegration behavior of scaffolds in hyaluronidase (100 U/mL). (K) Enzymatic degradation of scaffolds against type I collagenase (100 U/mL). PiHCLS denotes the analyzed scaffolds. The letter "*i*', with *i* = 1, 2, or 3 denotes the absence, the intermediate, and high levels of nHAP amounts, respectively. *n* = 3 independent experiments per group; the significance levels were established at $p < 0.05$ (*), $p < 0.01$ (**), and $p < 0.001$ (***), respectively.

among PLGA-HAP (PLGA, PLGA-HAP$_1$, and PLGA-HAP$_2$), HAD (Figure S3, Supporting Information), and Col I, while the HCLS group without PLGA-HAP was set as the control group. The PHCLS was formed as shown in Figure S4 and the hierarchical porous structure was visualized through SEM (Figure 2A) and calcein (Figure 2B) and H&E staining (Figure 2C) of the scaffold sections. As seen in the SEM images, all four sets of scaffolds had good porosity interconnectivity and homogeneous macroporous morphology, with interconnected pores measuring 238−380 μm and a frame wall thickness measuring 2−6 μm. (Figure 2A, left row). Interestingly, the macropore size varied among the four groups, and with the increase of nHAP content in PLGA-HAP, the pore size of the macropore and porosity decreased gradually (Figure 2D,F). Such result confirmed that more nHAP could chelate with the catechol group in the P$_3$HCLS group relative to other groups through free Ca^{2+},[5] resulting in a higher degree of cross-linking and more dense channels. At a higher magnification, PLGA-HAP was successfully embedded into the pore walls of the hydrogel scaffolds and achieved good interfacial integration between the matrix (Figure 2A, middle row). The pore structure integrity (pore size and hole wall thickness) of the microspheres was well preserved in these regions, where microsized pores (3.7−7.6 μm) were uniformly distributed throughout the surface of macropore walls (Figure 2A, right row and Figure 2E). PLGA-HAP maintained structural integrity and stability inside the PHCLS, in turn ensuring the achievement of the hierarchical microporous structure (Figures 2B,C and S5). nHAP was evenly distributed in both P$_2$HCLS and P$_3$HCLS groups according to the calcein staining results, and the pore size was smaller in the central region of the microspheres in P$_3$HCLS as compared to PHCLS and P$_2$HCLS groups, which was consistent with the above experimental results. Furthermore, according to the SEM and AFM results, certain content of nHAP provided a larger specific surface area and higher surface roughness, so the coprecipitation of cytokines and growth factors as well as ion exchange in contact with biological fluids were both made possible by the P$_2$HCLS, and these processes indirectly promoted BMSC migration. In summary, we found that the macropore size was well maintained in the hydrogel phase while PLGA-HAP were interspersed and embedded between the closed macropore walls, which further increased pore size diversity (3.7−380 μm) and enhanced pore communication inside the PHCLS, thus providing a "highway" of various scales for oxygen and nutrient transport during skull regeneration.

According to a definition of "particle reinforcement" that goes beyond the conventional definition, adding PLGA-HAP porous microspheres with various nHAP contents has a significant positive impact. DMA was used to calculate the scaffolds' storage and loss moduli. As shown in Figure 2G,H, the storage modulus rose with frequency, and the P$_2$HCLS (67.8 ± 5.3 kPa) and P$_3$HCLS (77.5 ± 4.9 kPa) had much greater storage and loss moduli than the other groups. The static compression mechanics tests of the HCLS, P$_1$HCLS, P$_2$HCLS, and P$_3$HCLS were also examined. Figure S6 demonstrates that the compression strength of the P$_2$HCLS and P$_3$HCLS was significantly greater than that of the HCLS and P$_1$HCLS ($p < 0.001$), which indicated that the addition of nHAP would boost the mechanical strength of hydrogel-based scaffolds. According to Figure S6A, the mechanical strength of every scaffold displayed the same pattern. The HCLS, P$_1$HCLS, P$_2$HCLS, and P$_3$HCLS had compressive moduli of

11.33 ± 2.12, 15.67 ± 4.36, 59.67 ± 6.41, and 87.43 ± 3.25 kPa, respectively (Figure S6B). Consequently, the P$_3$HCLS and P$_2$HCLS showed higher mechanical strength, which could provide better mechanical support for implantation. There were two probable explanations found. One is the standard particle reinforcement system load transfer effect.[37,38] The other factor has to do with the PLGA-HAP and hydrogel matrix's compatible interface. During the gelling process, they could create a stable hybrid cross-linked network at the interface, which would solve the incompatibility interface issue. Furthermore, the P$_2$HCLS and P$_3$HCLS were characterized by a tighter hybrid chemical cross-linked network. The mechanical strength of the hydrogels was correlated with the mesh size, which was defined as the separation between cross-linking points of the hydrogel network.[39]

The mesh size at the molecular level would be impacted by lyophilization; thus, lyophilized SEM samples could only be utilized to observe macropore size. As a result, the scaffolds' mesh size was determined using the rubber elasticity theory.[40] As seen in Figure S7, the P$_2$HCLS and P$_3$HCLS had mesh sizes that were smaller than those of the HCLS and P$_1$HCLS, further proving that the P$_2$HCLS and P$_3$HCLS had a more tightly knit network of hybrid chemical cross-links. The in vitro mineralization tests were conducted to determine bioactivity. SEM images suggested that microspherical osteoid apatite agglomerates were dispersed on the surface of the P$_2$HCLS in contrast to the morphology of the apatite deposited by bone cell action, and high-magnification images showed that all of the osteoid apatite particles had nanolath-like structures, a typical HAP crystal (Figure S8A).[41] EDS examination showed that the majority of the elements in the crystals were Ca and P, with a Ca/P ratio of 2.51, which was similar to mineralized HAP in natural bone (Figure S8B).[42] These findings point to the significant osteogenic activity of the P$_2$HCLS, which may encourage the profuse mineralization and deposition of the bone matrix within the scaffold. After 52 h, P$_2$HCLS and P$_3$HCLS' swelling equilibrium was attained, and the swelling ratio of the P$_2$HCLS (23%) and P$_3$HCLS (21%) was significantly lower than that of the P$_1$HCLS (29%) and HCLS (33%) as shown in Figure 2I. This might be attributed to the charged groups in the PiHCLS, which were responsible for water uptake and might be occupied due to interactions of the polymers with increasing nHAP content. Subsequently, the degradation behavior of scaffolds was also evaluated. As shown in Figure 2J,K, the P$_2$HCLS and P$_3$HCLS degraded smoothly both in hyaluronidase and type I collagenase solution and reached degradation equilibrium after 120 and 136 h, respectively. The cross-linking network created by the Michael addition reaction between phenolic hydroxyl groups on HAD and amino groups on Col I was disrupted when hyaluronidase cracked HAD or collagenase damaged Col, so the HCLS dissolved more quickly than the other two groups. Regarding the degradation rate, the cross-linking network contained HAD and Col I alike in all groups while the presence of more nHAP formed a denser cross-linked network and restricted the accessibility of enzymes. The delayed degradation rate in the PHCLS might also provide the continuous process of bone regeneration, thus enhancing its clinical translatability.

3.3. PHCLSs Promote BMSC Proliferation, Migration, and Differentiation In Vitro. To determine the impact of the newly introduced hierarchical microporous structure on osteogenic activity, all four groups of scaffolds were cocultured with BMSCs for 3, 7, and 14 days. Each group was then
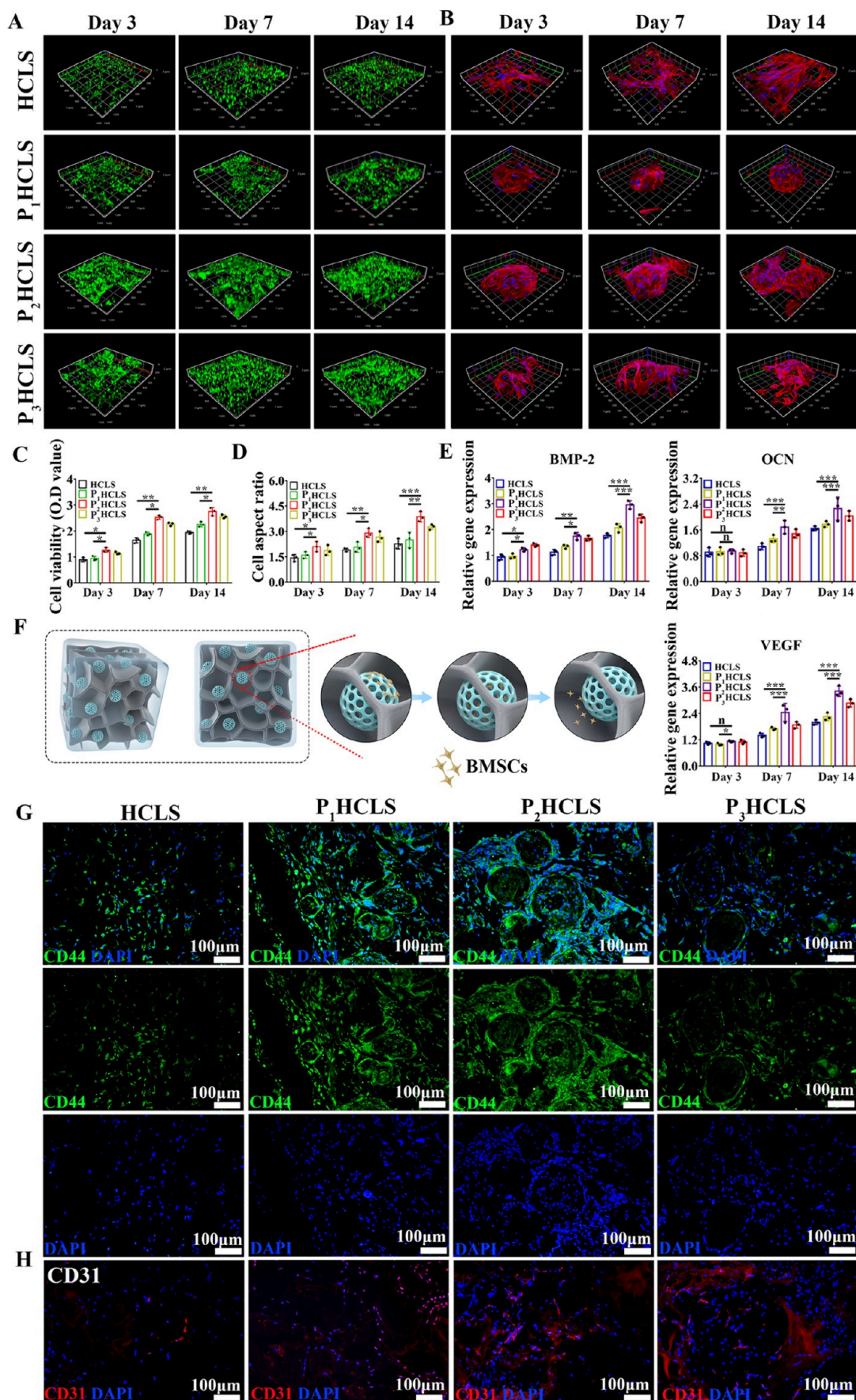
Figure 3. PHCLS enhances in vitro BMSC migration, proliferation, and differentiation. (A) Live/dead staining and (B) BMSC-loaded scaffolds were stained for the cytoskeleton on days 3, 7, and 14. (C) CCK-8 was used to assess the viability of BMSCs on various scaffolds at 3, 7, and 14

Figure 3. continued

days. (D) Quantitative cell aspect ratio based on CLSM images of cytoskeleton staining. (E) Relative expression of BMP-2, OCN, and VEGF showing osteogenesis and angiogenesis levels. (F) Schematic diagram of the hierarchical microporous structure promoting BMSC migration. (G) IF staining of CD44 at day 14 showing remarkable BMSC infiltration and migration in P_2HCLSs. (H) CD31 IF staining at day 14 revealed more early angiogenesis in P_2HCLSs. n = 3 independent experiments per group; the significance levels were established at $p < 0.05$ (*), $p < 0.01$ (**), and $p < 0.001$ (***), respectively.
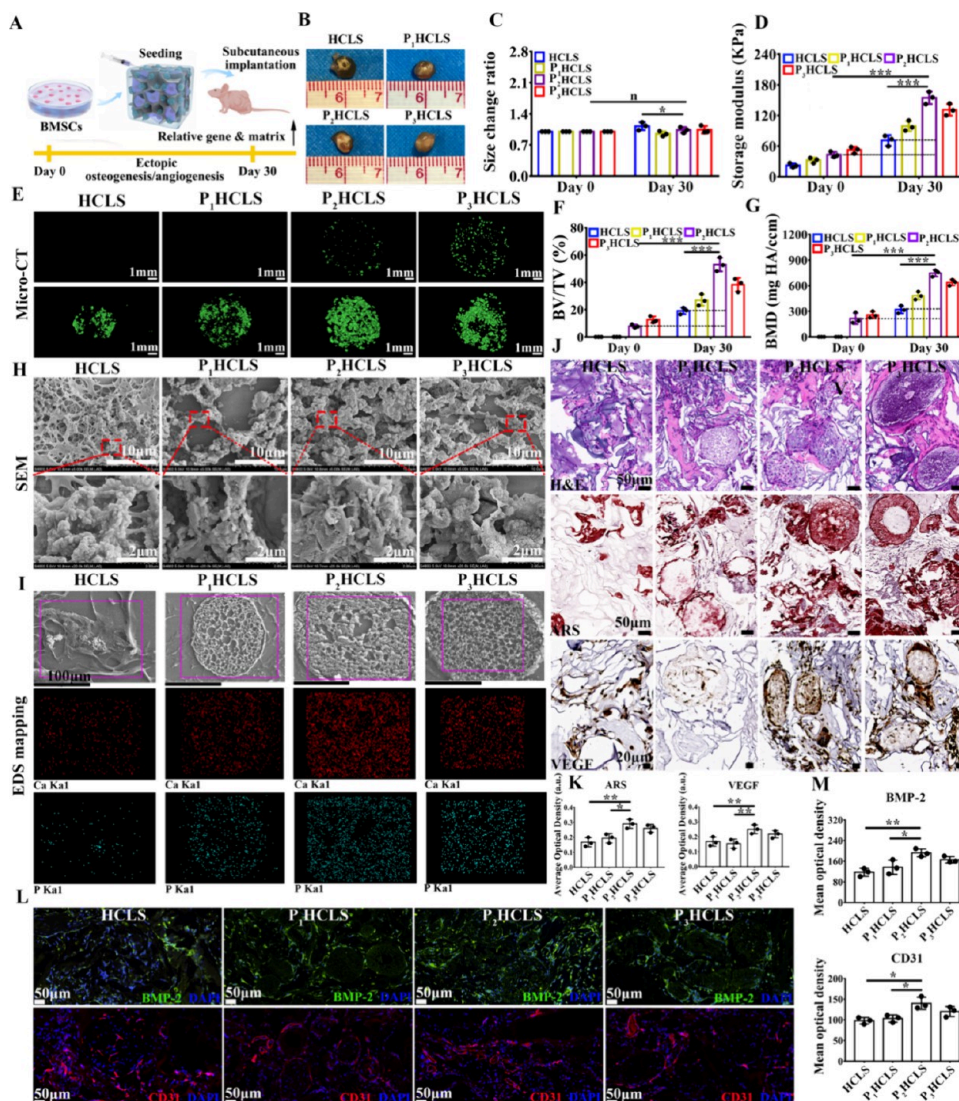
Figure 4. Different scaffolds used in a subcutaneous implantation model for ectopic angiogenesis and osteogenesis evaluation. (A) Experimental design for ectopic angiogenesis and osteogenesis. (B) Gross appearance of the samples after 30 day implantation. (C) Dimensional data on various scaffolds both before and after installation. (D) Compressive storage modulus of various scaffolds reveals mechanical improvements. (E) Images of 3D reconstruction taken by micro-CT of different specimens both before and after implantation. (F) Bone mineral density (BMD) and bone volume fraction (BV/TV) results in the semiquantitative form. (H) SEM images of the sample slices from different samples. (I) Images from EDS mapping demonstrating ectopic mineralization of different scaffolds. (J) IHC staining of H&E, ARS, and VEGF in different sample sections (V: new blood vessels). (K) Semiquantitative results of ARS and VEGF staining based on ImageJ software. (L) BMP-2 and CD31 IF labeling at day 30 reveals increased early angiogenesis and osteogenesis in P_2HCLSs. (M) Semiquantitative IF staining results. n = 3 independent experiments per group; the significance levels were established at $p < 0.05$ (*), $p < 0.01$ (**), and $p < 0.001$ (***), respectively.

subjected to live/dead staining (Figure 3A) and cytoskeleton staining (Figure 3B). The scaffolds had an acceptable level of biocompatibility, as evidenced by the lack of any obvious dead cells and the progressive growth of live cells. The number of cells gradually grew as the culture time was extended (from 3 to 14 days), and the growth tendency of the P_2HCLS group became more apparent, indicating that the newly introduced hierarchical microporous structure provided an improved

microenvironment for cell growth. The CCK-8 data confirmed this conclusion (Figure 3C). All of the BMSCs in the scaffolds were able to maintain an excellent cell spreading pattern for 3–14 days, which may strongly support the stem cell phenotype. Interestingly, distinct spherical-oriented growth was observed on the P_2HCLS due to the PLGA-HAP growth areas. In addition, the BMSCs in the P_2HCLS had a higher cell aspect ratio (Figure 3D), suggesting that the P_2HCLS promoted

BMSC proliferation, adhesion, and spreading along with its hierarchical microporous structure.

To evaluate BMSCs' osteogenic and angiogenic differentiation after 3, 7, and 14 days of in vitro coculturing, the expression levels of genes related to early-stage osteogenesis (biomineralization associated BMP-2), angiogenesis (VEGF), and late-stage osteogenesis (OCN) were assessed by RT-PCR (Figure 3E). All genes' expression gradually rose up to day 14, but mainly BMP-2 and VEGF expressions were significantly higher on day 14 than on day 7 at this point. The BMP-2 gene expression in the P_2HCLS was slightly higher than those in the P_1HCLS and HCLS at day 3 and it significantly surpassed these two groups with the extension of cocultured time. At day 3, there was no discernible difference in the expression of the OCN and ANC genes between the HCLS and P_2HCLS, but as time went on, the P_2HCLS group showed a clear ascending tendency, suggesting that the long-term maintenance effect of hierarchical microporous structural design on angiogenesis/osteogenesis might be improved. Meanwhile, we hypothesized that the hierarchical microporous design of the PHCLS could open up the hydrogel scaffold-sealed pore wall structure, improve pore communication, and increase the diversity of pore size inside the scaffold. The micropores were important to allow for a flux of O_2 and nutrients. BMSC migration would be facilitated by 3D hierarchical microporous scaffolds that might offer different scales of transportation "highways" for the transportation of oxygen, nutrients, and even metabolic products (Figure 3F). Samples cocultured with BMSCs for 14 days were sectioned, and CD44 IF staining was performed to confirm our hypotheses (Figure 3G). Compared with the single pore size distribution of hydrogel scaffolds (HCLS), the hierarchical microporous scaffolds (P_2HCLS) significantly promoted the migration of BMSCs (Figure S9), which was consistent with our hypothesis. To further intuitively evaluate the angiogenetic differentiation of BMSCs, we performed CD31 IF staining on different specimens on day 14 (Figures 3H, S9, and S10). CD31-positive expression cells were found in all four groups of samples. According to the cell number, a normalized semiquantitative analysis of CD31 IF staining revealed that the P_2HCLS displayed greater positive staining, which was consistent with the analysis's findings, as shown in Figure 3E. To further prove the expression levels of osteoblast-related proteins and calcium deposition in vitro, ALP and ARS staining of different sample sections was performed at day 14. At day 14, all groups demonstrated favorable results, as shown in Figure S11A, with the P_2HCLS group exhibiting the greatest ALP staining at the time periods (Figure S11C). To analyze the mineral deposition of BMSCs in the scaffolds, ARS staining was performed on day 14. As shown in Figure S11B, all groups showed positive ARS staining results, and the highest mineralization level with densified distribution of calcium nodules was presented in the P_2HCLS group (Figure S11C). These findings demonstrated that BMSC proliferative, migratory, and angio/osteogenetic differentiation in vitro might be stimulated by the P_2HCLS. In addition, we observed markedly increased cell migration and a higher expression of the vascular marker CD31 in the P_2HCLS when compared to the denser P_3HCLS. This problem could not be solved by merely increasing cross-linking density by increasing the concentration of nHAP in the P_3HCLS to improve its G' because this made the scaffold impermeable to cell infiltration and migration. Even though PLGA-HAP$_1$ only had a 12.1% w/w nHAP loading, we thought it would have a significant impact

on the pore size distribution in the P_2HCLS. The hierarchical microporous structure of the P_2HCLS and the conditioning of polyphenols were responsible for the cell infiltration and angiogenic property, although the presence of nHAP also seemed to encourage cell movement (Figure 3F−H). The P_2HCLS's macropore (∼300 μm) may also be helpful for the passage of suture wires that firmly bind the implant to the patient's host bone, improving its clinical translatability.

3.4. PHCLSs Enhance Ectopic Angiogenesis and Osteogenesis in the Subcutaneous Implantation Model. BALB/c nude mice were subcutaneously implanted with BMSC-laden scaffolds (containing HCLS, P_1HCLS, P_2HCLS, and P_3HCLS) for 30 days to model bone matrix formation and mineralization (Figure 4A). On day 30, all scaffolds displayed varying degrees of mineralization and were partially merged with the surrounding tissue (Figure 4B). Figure 4C presents statistics for the ratio of size changes before and after implantation. After implantation, the HCLS group showed a considerable dimensional increment (1.07 ± 0.16); however, the P_2HCLS did not show any significant size changes (0.97 ± 0.08), suggesting the structural stability of BMSC-laden P_2HCLSs in vivo. Because bone matrix deposition has the potential to strengthen implants, samples were exposed to the DMA compression test before and after implantation to evaluate mechanical augmentation (Figure 4D). In line with the findings of Figure 2H, the P_3HCLS demonstrated a storage modulus much greater than that of the HCLS prior to implantation, demonstrating that chemically integrating PLGA-HAP$_2$ improved the mechanical properties. Intriguingly, the storage modulus of the P_2HCLS (153.0 ± 9.0 kPa) was approximately four times its starting value (also in comparison to the HCLS, P_1HCLS, and P_3HCLS at 66.0 ± 8.0, 96.0 ± 5.0, and 124.0 ± 7.0 kPa, respectively), suggesting increased mineralization and bone matrix deposition inside the P_2HCLS.

The largest amount of minerals was consistently deposited inside the P_2HCLS, while the center of the P_3HCLS was hollow, according to a micro-CT 3D reconstruction (Figure 4E). More apatite was deposited in the P_2HCLS, according to quantitative measurement of the bone volume fraction (BV/TV) and bone mineral density (BMD) (56.5 ± 4.3% and 737.1 ± 15.2 mg of HAP/ccm) (Figure 4F,G). The SEM result also supported the mineralization trend (P_2HCLS > P_3HCLS > P_1HCLS > HCLS; $p < 0.001$; Figure 4H). In particular, the hierarchical microporous structure was still maintained in the P_2HCLS even though there were large amounts of mineralized deposits. On the hole wall of PLGA-HAP in the P_2HCLS, which was quite comparable to the structure of the natural bone matrix, there were some mineral nanoparticles with an average size of around 200 nm that were dispersed equally.[43] With a Ca/P ratio of 1.86 ± 0.22, the EDS result of the P_2HCLS showed a homogeneous and dense distribution of Ca and P components that were the closest to that of normal bone tissue (1.67; Figure 4I).

Histological, IHC, and IF stainings were conducted in order to more intuitively assess the angio- and osteogenetic differentiation of BMSCs (Figure 4J−M). Benefiting from the hierarchical microporous structure of the P_2HCLS, a large number of BMSCs infiltrated and migrated into the scaffolds along with newly formed bone growth and revascularization according to H&E staining (Figure 4J). ARS and BMP-2 stainings and their corresponding semiquantitative data (Figures 4K,M and S12) further confirmed more calcium
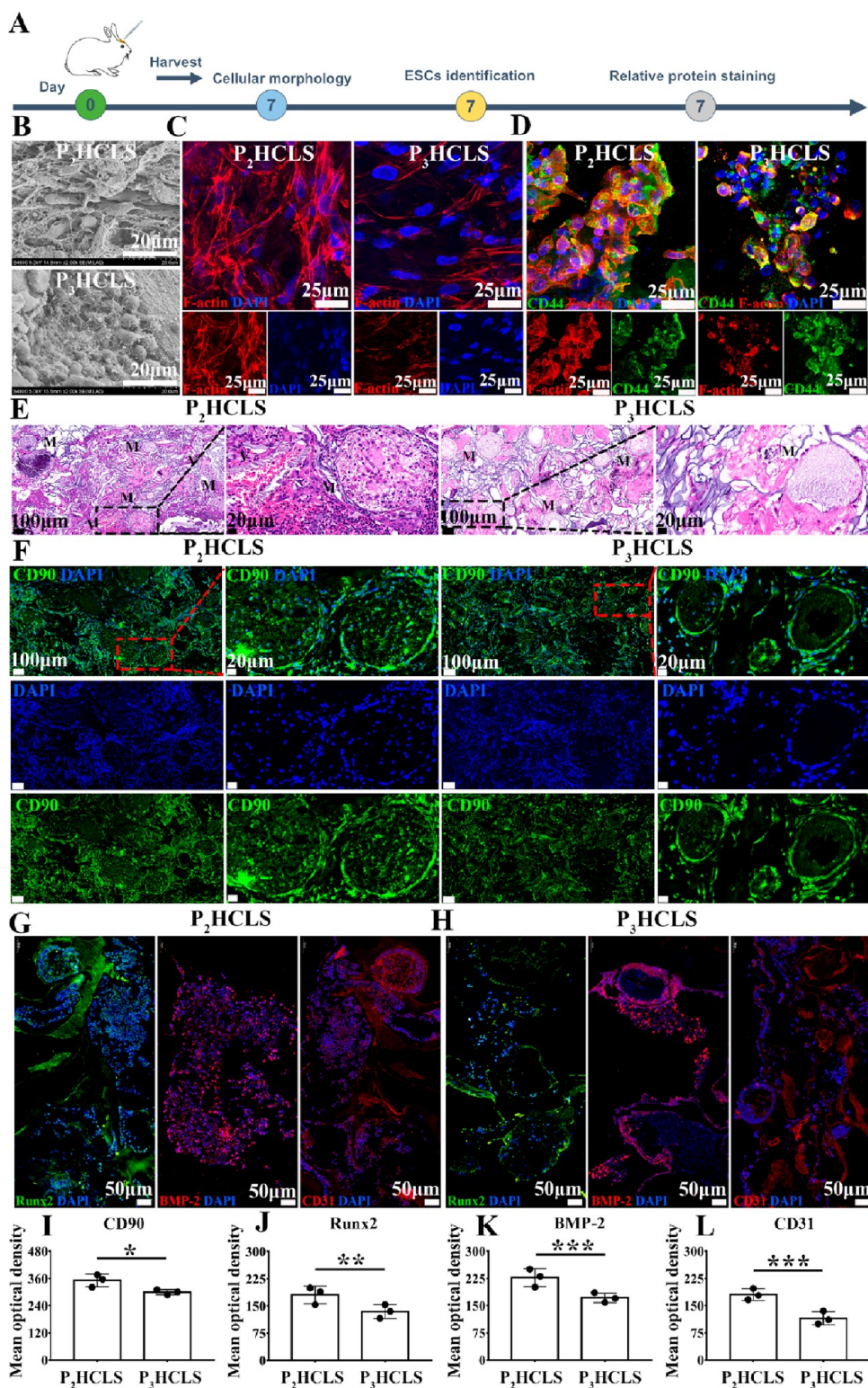
Figure 5. PHCLSs promote angiogenesis and early osteogenesis by accelerating ESC recruitment in vivo. (A) Experiment diagram for cell recruitment. (B) ESC cytoskeleton staining in various scaffolds. (C) CLSM pictures of ESCs stained with CD44/F-actin/DAPI in various scaffolds. (D) H&E staining of diverse scaffolds after 30 days of implantation (V: new blood vessels; M: microspheres). (E) CLSM images of CD90 IF staining of the samples. (F, G) Runx2, BMP-2, and CD31 IF staining after a week of various treatments. (H−K) Corresponding semiquantitative results of IF staining by using ImageJ software ($n = 3$, the number of pictures per specimen analyzed for the semiquantive analysis). $n = 3$ independent experiments per group; the significance levels were established at $p < 0.05$ (*), $p < 0.01$ (**), and $p < 0.001$ (***), respectively.

nodules and BMP-2 positive expression cells in the P_2HCLS, which suggested that the P_2HCLS could provide a more favorable microenvironment for osteodifferentiation. Indeed, in

nude mice, the BMSC-loaded P_2HCLS demonstrated considerable ectopic mineralization and angiogenesis, as well as extremely consistent osteoid matrix development (Figure 4E−
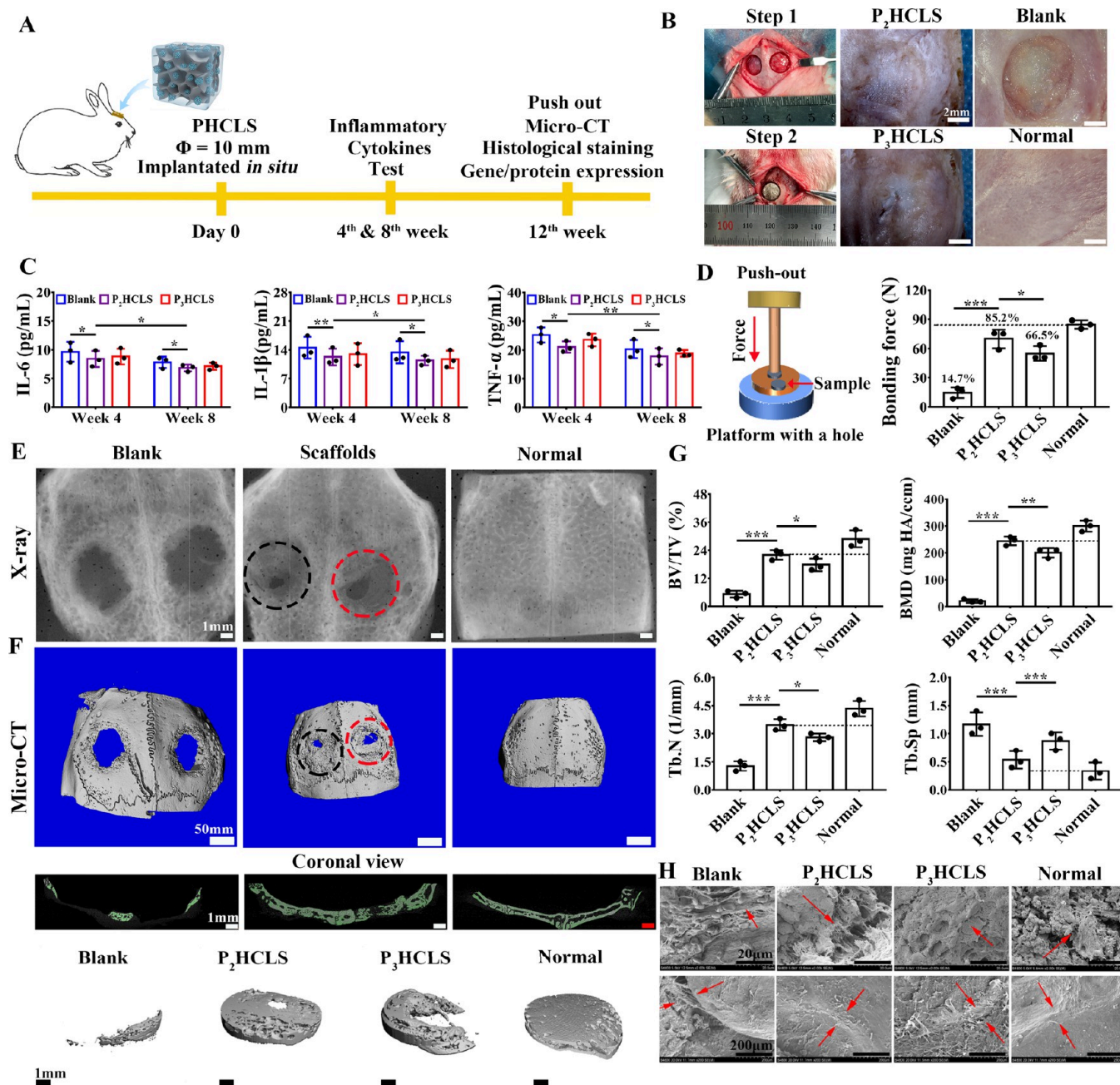
Figure 6. PHCLSs accelerate bone regeneration in a critical-size rabbit skull defect model. (A) Diagram of the schematic on in vivo bone restoration. (B) Surgical procedure and a gross image of the repaired skull defect at week 12. (C) Inflammatory cytokine IL-6, IL−1β, and TNF-α expression at week 4 and 8. (D) Mechanical push-out test and interface binding strength between distinct groups of new bone and host tissue. (E) X-ray pictures of various treatment groups 12 weeks after implantation. (F) Coronal view and representative micro-CT 3D reconstruction of various treated groups after 12 weeks of implantation. (G) Quantitative analyses of micro-CT results at week 12. (H) SEM images of the defect in various treatment groups at week 12 showing the cross-section and interface between host tissue and various scaffolds. n = 3 independent experiments per group. The significance levels were established at $p < 0.05$ (*), $p < 0.01$ (**), and $p < 0.001$ (***), respectively.

M). A coordinated osteogenic and angiogenic response is needed at the repair site for bone defect healing, which is a dynamic progenitor cell-driven tissue morphogenetic process.[44] As a result, vascularization is also necessary for successful bone repair. Curiously, both the macro- and micropores of the P$_2$HCLS showed more pronounced positive staining for VEGF and endothelial cell markers (CD31) (Figures 4L,M and S12), indicating that our polyphenol-mediated hierarchical microporous structure of the P$_2$HCLS promoted the infiltration and migration of BMSCs, and this resulted in increased amounts of

released proangiogenic molecules, such as BMP-2 and VEGF, to remodel the matrix and promote angiogenesis within the implant.

3.5. PHCLSs Promote Angiogenesis and Early Osteogenesis by Accelerating ESC Recruitment. It has been difficult to fully rebuild critical-size skull defects using cell-free scaffolds alone, because spontaneous endogenous cell infiltration to reconstruct cranial tissue is a lengthy, laborious process. It would be significantly valuable if the P$_2$HCLS could facilitate ESC recruitment. As a result, on day 7, cell-free P$_2$HCLSs and

P_3HCLSs were removed from rabbit cranial critical-size defects (Φ = 10 mm) for evaluation (Figure 5A). In comparison to attached spherical cells in the P_3HCLS group, cell morphology on scaffolds detected by SEM in the P_2HCLS group exhibited equally distributed fusiform shape cells, and the cytoskeletal staining images further verified the spreading cell morphology (Figure 5B). Significant elongated actin filaments (red) and CD44 positive expression (green) around the cell nuclei (blue) were visible in the CLSM pictures, which supported the ESCs' apparent attachment and proliferation in the P_2HCLS (Figure 5C). On day 7, H&E staining (Figure 5D) revealed that the P_2HCLS had attracted more endogenous cells than the P_3HCLS. Additionally, the P_2HCL group displayed superior cellular infiltration and neovascularization, demonstrating that the hierarchical micropore architecture in the P_2HCLS provided a better milieu for cellular infiltration and angiogenesis. By contrast, in the P_3HCLS, we found that the endogenous cells could only congregate on the edge of PLGA-HAP and were unable to penetrate it adequately. On day 7, IF labeling for the stem cell surface marker cluster of differentiation 90 (CD90) showed that more cells with positive expression not only migrated into the micropore but also infiltrated the macropore in the P_2HCLS group, while just a few were seen in the P_3HCLS group (Figure 5E,H). This result highlighted the significance of the interconnected hierarchical pore network in facilitating ESC recruitment and angiogenesis in vivo.

On day 7, IF staining was used to further assess the scaffolds' ability to promote angiogenesis and osteogenesis. Runt-related transcription factor 2 (Runx2) is a particular transcription factor necessary for bone formation that controls BMSCs' ability to develop into osteoblasts, prevents this ability from occurring when they would otherwise differentiate into chondrocytes and adipocytes, and regulates the expression of matrix genes including OCN and Col I.[45] By using IF staining, it was possible to identify positive Runx2 in the P_2HCLS and P_3HCLS groups (Figure 5F,G, left column; Figure S13), and semiquantitative analysis further showed that Runx2 was expressed more abundantly in the P_2HCLS group (Figure 5I), demonstrating its potential for osteoinduction. Col I matrix production and BMP-2 secretion are both elevated during the early differentiation stage. After 1 week of implantation, the P_2HCLS group demonstrated noticeably higher expression of BMP-2 than the P_3HCLS group (Figure 5F, middle column; Figures 5J and S13). In the P_2HCLS, CD31 expression was also increased (Figure 5F, right column; Figures 5K and S13), which indicated considerable potential for early osteogenesis and blood vessel formation. By promoting autologous stem cell recruitment and angiogenesis, this work emphasizes the use of the body's own capacity for skull remodeling and regeneration. Rapid vascularization and early osteogenesis by recruiting ESCs in situ were detected inside the scaffold, together with a greater expression of angio/osteogenic associated factors, even in the absence of foreign cells or cytokines loaded into the P_2HCLS prior to implantation. Contrarily, the majority of current research has focused on the utilization of exogenous components or cellular cues in conjunction with scaffolds. The effects of cellular infiltration and vascularized bone regeneration were minimal even with the addition of these components. The main promotion in this process might be the hierarchical micropores. The "initial hierarchical micropore acceleration" that we characterize as occurring during the early stages of

regeneration could be attributable to the following three factors: first, the P_2HCLS could facilitate ion exchange when in contact with biological fluids as well as the coprecipitation of endogenous cytokines and growth factors, which indirectly stimulate stem cell recruitment to the defect site by offering a larger specific surface area and higher surface roughness. Second, the macropore (100–500 μm) is necessary to promote ESC migration to the scaffold for a longer period of time, achieve superior osseointegration, and promote bone ingrowth. Last but not least, our recently published research demonstrated that the polyphenol-integrated nanointerface between the fibrillar matrix and nHAP may drive functional cell/cytokine adhesion, incipient vascularization, and significantly increase ESC recruitment to start robust osteogenesis.[6]

3.6. PHCLSs Facilitate Bone Regeneration in Critical-Size Cranial Defects in Rabbits.
At week 12, bone regeneration potential of cell-free P_2HCLSs and P_3HCLSs was assessed after being implanted in situ (rabbit cranial critical-size defect, Φ = 10 mm; Figure 6A). Figure 6B shows the surgical procedure and a broad view of the defect area at week 12. After 12 weeks of implantation, large volumes of new bone tissue were seen and were well integrated with the surrounding tissue in the P_2HCLS group, whereas there was essentially no progress made in the healing process in the blank group, indicating the clinical research value of this animal model. In the P_2HCLS group, inflammatory cytokine levels (IL-6, IL-1β, and TNF-α) were lower than those in the blank group (Figure 6C). Furthermore, they were dramatically downregulated after 8 weeks of implantation, demonstrating that the P_2HCLS was biosafe and did not produce severe inflammatory reactions. The interfacial bonding force between the host and new bone tissue was then assessed at week 12 by using the push-out test (Figure 6D). In contrast to the P_3HCLS ($p < 0.05$) and blank group ($p < 0.001$), the breaking load between the P_2HCLS and host bone tissue was 73.7 ± 13.5 N (reaching 85.2% of the normal group).

X-ray was used to visualize the effect of the P_2HCLS in facilitating skull reconstruction (Figure 6E) and the result showed only limited bone formation at the margins in the blank group, while the P_2HCLS group facilitated the formation of new bone with a bone cover area that was similar to natural bone. The 3D reconstruction results by micro-CT were consistent with the radiographic images (Figure 6F, first row). Coronal pictures of micro-CT analysis demonstrated the development of new bone around the edges of defects (Figure 6F, middle row), which had already grown to the center of the bone cavity in the P_2HCLS and established a nearly complete bone structure at week 12. However, the P_3HCLS group still had clear and noticeable defects. Only a small quantity of new bone developed along the defect edge in the blank group. The regenerated bone in the defect area was next subjected to a 3D reconstruction and a semiquantitative examination (Figure 6F, third row and Figure 6G). The findings revealed that the P_2HCLS group had BV/TV (22.1 ± 1.7%; 78.6% of natural bone), BMD (232.09 ± 13.25 mg HAP/ccm), and trabecular number (Tb·N at 3.39 ± 0.31 mm^{-1}) values that were considerably higher than those of the control groups but with significantly lower trabecular separation (Tb·Sp at 0.5746 ± 0.1218 mm) compared to the P_3HCLS (BV/TV: 16.9 ± 4.2%; BMD: 197.51 ± 15.37 mg HAP/ccm; Tb·N: 2.86 ± 0.12 mm^{-1}; and Tb·Sp: 0.6814 ± 0.1095 mm) and blank group (BV/TV: 5.4 ± 0.9%; BMD: 21.11 ± 5.37 mg HA/ccm; Tb·N: 1.32 ± 0.38 mm^{-1}; and Tb·Sp: 1.1806 ± 0.2125 mm), which
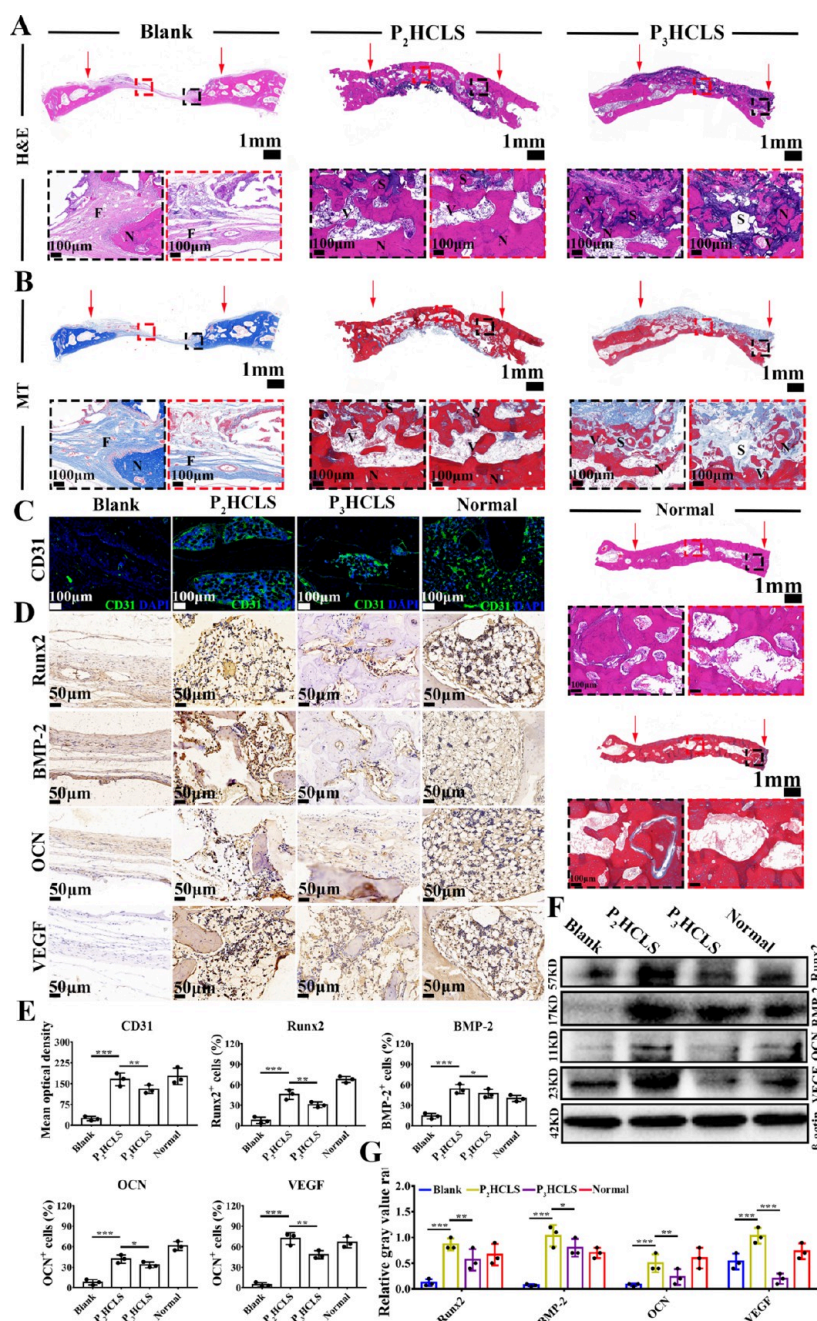
Figure 7. Evaluation of histology and postimplantation protein expression. (A) Images of different treated groups stained with H&E after 12 weeks of implantation. (B) Images of MT staining from various treated groups at week 12 (Row 1: General assessment of the skull defect regeneration. The red arrow denotes the defect's starting boundaries. Row 2: A magnified picture of the defect's center and perimeter site). N stands for new bone tissue; S is for scaffold; V stands for new blood vessels; and F stands for fibrous tissue. (C) Different groups' regenerated vessels were stained with CD31 IF at week 12. (D) Representative immunohistochemical pictures of Runx2, BMP-2, OCN, and VEGF were taken at week 12 following implantation. (E) Analysis of positive cell numbers and CD31 IF staining at week 12. (all scaffolds are devoid of cells. Blank: no treatment for the defect). (F) WB examination of the expression of Runx2, BMP-2, OCN, and VEGF in various treatment groups. (G) WB examination of the relative content (gray value ratio) of Runx2, BMP-2, OCN, and VEGF protein in various scaffolds at week 12. $n = 3$ separate experiments per group; the significance levels were established at $p < 0.05$ (*), $p < 0.01$ (**), and $p < 0.001$ (***), respectively.

were significantly more resemblant of the normal group. These findings showed that the P$_2$HCLS performed well in terms of bone regeneration in a rabbit cranial critical-size defect. Typical mineralized tissue morphology was visible in the SEM pictures of cross-sections at defect sites in the P$_2$HCLS group, which was more comparable to natural bone tissue than in the P$_3$HCLS group. However, there was only fibrous tissue without significant mineralization in the blank groups (Figure 6H, first

row). In addition, the dense and smooth interface in the P$_2$HCLS was close to that of the normal group, suggesting good osteointegration ability (Figure 6H, second row). In conclusion, such rapid initiation of vascularized osteogenesis by this "initial hierarchical micropore acceleration", together with the polyphenol-mediated interface integration, resulted in a more rapid progression of bone remodeling in the P$_2$HCLS group. These results implied the potential of polyphenol-

mediated hierarchical microporous scaffolds for bone regeneration. Aside from the findings reported here on the P$_2$HCLS's unique structural design, composition, and properties, the great safety track record of HA, Col I, nHAP, and PLGA in clinical devices argues in favor of the scaffold's eventual clinical translation.

Following this, the tissues were sectioned and stained with H&E and MT to further assess the regeneration impact (Figure 7A,B). The results demonstrated that at week 12, in the P$_2$HCLS treatment groups, a significant volume of mature, dense bone tissue totally colonized the defect area and closely merged with the host bone. The P$_2$HCLS, which had a rather full laminar structure resembling the real skull, showed neovascularization, bone lacunas, and central canals (Figure 7A). Even after 12 weeks, fibrous tissue predominated in the blank group, and just a little amount of newly produced bone appeared in the defect perimeter. The largest area of strong mature collagen (red areas) in the P$_2$HCLS after 12 weeks revealed excellent osteogenic potential, while there was no discernible collagen fiber synthesis in the blank group according to MT staining (Figure 7B). Then, by positive CD31 staining, scaffold-mediated host cell angiogenic differentiation was shown in vivo (Figures 7C and S14). At postoperative week 12, both the P$_2$HCLS and P$_3$HCLS groups experienced infiltration by host vascular endothelial cells (CD31$^+$) that led to neovascularization. The P$_2$HCLS, however, displayed a higher positive expression (Figure 7E) and was well developed with continuous endothelial lining cells that more closely resembled the natural group. These outcomes supported the hypothesis that the P$_2$HCLS enhanced host blood vessel ingrowth and promoted skull repair. IHC staining findings showed that the P$_2$HCLS group had higher levels of positive Runx2, BMP-2, OCN, and VEGF expression than the blank ($p < 0.001$) and P$_3$HCLS ($p < 0.05$) groups (Figure 7D,E), suggesting that the P$_2$HCLS could genetically encourage vascularization and bone regeneration in situ. Additionally, the western blot (WB) of important osteogenic and angiogenic proteins (Runx2, BMP-2, OCN, and VEGF) showed that the P$_2$HCLS group had higher expression than the blank ($p < 0.001$) and P$_3$HCLS ($p < 0.05$) groups, which was compatible with the results of IHC staining (Figure 7F,G). The WB results also supported P$_2$HCLS's better ability for promoting osteovascularization.

4. CONCLUSIONS

In conclusion, we have developed a hybrid interleaving hierarchical microporous scaffold by polyphenol-mediated interface integration between the hydrogel matrix and PLGA-HAP open porous microspheres via the Michael addition reaction and Ca^{2+} chelation. The hierarchical microporous structure not only improved the diversity of pore size and pore communication inside the scaffold but also greatly enhanced its mechanical and degradation properties. The in vitro and in vivo results demonstrated that the interconnected pore network and polyphenol-mediated interface integration accelerated BMSC proliferation, migration, and angio/osteogenic response within the P$_2$HCLS and facilitated ESC homing and early angiogenic/osteogenic differentiation without any extraneous cells or factors. Benefiting from structure and components similar to the cranial bone, significant ectopic vascularized bone regeneration and in situ skull reconstruction were achieved by the scaffold. Our objective is to transform

this new approach into the best possible treatment for the many individuals who are experiencing bone loss.

■ ASSOCIATED CONTENT

ⓢ Supporting Information

The Supporting Information is available free of charge at https://pubs.acs.org/doi/10.1021/acs.biomac.3c00655.

Primers used to amplify mRNAs encoding rabbit GAPDH; characterization of microspheres' surface roughness; Ca^{2+} release from the P$_2$HCLS and P$_3$HCLS groups during different periods; ^{1}H NMR (D$_2$O) spectra of HAD and dopamine; representative stereomicroscopy images of different scaffolds; H&E staining of sample sections observed by optical microscopy; the static compression mechanics test of different scaffolds; the mesh size of various scaffolds calculated by storage modulus; the bioactivity measurements of the P$_2$HCLS in SBF at 37 °C for 7 days; normalized semiquantitative analysis of CD44 and CD31 IF staining according to the cell number by image J software; IF staining of CD31 after 14 days of coculturing with BMSCs in various scaffolds; IHC staining of osteogenic proteins and the characterization of calcium deposition in vitro; IF staining of BMP-2 and CD31 after 30 days subcutaneous implantation in nude mice; Runx2, BMP-2, and CD31 IF staining after 1 week's implantation in rabbit critical-size cranial defects; and CD31 IF staining of different treatments after 12 weeks' implantation in rabbit critical-size cranial defects (PDF)

■ AUTHOR INFORMATION

Corresponding Authors

Gonggong Lu − *Department of Neurosurgery, West China Hospital, Sichuan University, Chengdu, Sichuan 610041, P.R. China; National Engineering Research Center for Biomaterials and College of Biomedical Engineering, Sichuan University, Chengdu, Sichuan 610064, P.R. China;* ⓞ orcid.org/0009-0001-2133-489X; Email: Lugonggong@scu.edu.cn

Ugo D'Amora − *National Research Council, Institute of Polymers, Composites and Biomaterials, Naples 80125, Italy;* ⓞ orcid.org/0000-0002-6142-059X; Email: ugo.damora@cnr.it

Authors

Xiang Li − *Department of Neurosurgery, West China Hospital, Sichuan University, Chengdu, Sichuan 610041, P.R. China*

Peilei Wang − *National Engineering Research Center for Biomaterials and College of Biomedical Engineering, Sichuan University, Chengdu, Sichuan 610064, P.R. China*

Xing Li − *National Engineering Research Center for Biomaterials and College of Biomedical Engineering, Sichuan University, Chengdu, Sichuan 610064, P.R. China*

Yuxiang Wang − *National Engineering Research Center for Biomaterials and College of Biomedical Engineering, Sichuan University, Chengdu, Sichuan 610064, P.R. China*

Jiayi Zhu − *National Engineering Research Center for Biomaterials and College of Biomedical Engineering, Sichuan University, Chengdu, Sichuan 610064, P.R. China*

Alfredo Ronca − *National Research Council, Institute of Polymers, Composites and Biomaterials, Naples 80125, Italy*

Wenke Liu − *Department of Neurosurgery, West China Hospital, Sichuan University, Chengdu, Sichuan 610041, P.R. China*

Xuhui Hui − *Department of Neurosurgery, West China Hospital, Sichuan University, Chengdu, Sichuan 610041, P.R. China*

Complete contact information is available at:
https://pubs.acs.org/10.1021/acs.biomac.3c00655

Author Contributions

G.L. implemented all the experimental work, data analysis, manuscript writing, and funding acquisition. X.L., P.W., X.L., Y.W., J.Z., and W.L. assisted the experiments and discussed and modified the manuscript. U.D., A.R., and X.H. designed the project, supervised the research, and modified the manuscript.

Notes

The authors declare no competing financial interest.

■ REFERENCES

(1) Armiento, A. R.; Hatt, L. P.; Rosenberg, G. S.; Thompson, K.; Stoddart, M. J. Functional biomaterials for bone regeneration: A lesson in complex biology. *Adv. Funct. Mater.* **2020**, *30*, No. 1909874.

(2) Du, Y.; Guo, J. L.; Wang, J.; Mikos, A. G.; Zhang, S. Hierarchically designed bone scaffolds: From internal cues to external stimuli. *Biomaterials* **2019**, *218*, No. 119334.

(3) Pruett, L. J.; Jenkins, C. H.; Singh, N. S.; Catallo, K. J.; Griffin, D. R. Heparin Microislands in Microporous Annealed Particle Scaffolds for Accelerated Diabetic Wound Healing. *Adv. Funct. Mater.* **2021**, *31*, No. 2104337.

(4) Lu, G.; Xu, Y.; Liu, Q.; Chen, M.; Sun, H.; Wang, P.; Li, X.; Wang, Y.; Li, X.; Hui, X.; Luo, E.; Liu, J.; Jiang, Q.; Liang, J.; Fan, Y.; Sun, Y.; Zhang, X. An instantly fixable and self-adaptive scaffold for skull regeneration by autologous stem cell recruitment and angiogenesis. *Nat. Commun.* **2022**, *13*, 2499.

(5) Tong, L.; Pu, X.; Liu, Q.; Li, X.; Chen, M.; Wang, P.; Zou, Y.; Lu, G.; Liang, J.; Fan, Y.; Zhang, X.; Sun, Y. Nanostructured 3D-Printed hybrid scaffold accelerates bone regeneration by photo-integrating nanohydroxyapatite. *Adv. Sci.* **2023**, *10*, No. 2300038.

(6) Li, X.; Li, Z.; Wang, P.; Lu, G.; Tong, L.; Liu, Q.; Chen, Y.; Lin, J.; Luo, E.; Liang, J.; Jiang, Q.; Fan, Y.; Zhang, X.; Sun, Y. Dopamine-Integrated nanointerface between fibrillar matrix and hydrophilic nanohydroxyapatite regulates immune microenvironment to boost endogenous bone regeneration. *Adv. Funct. Mater.* **2023**, *33*, No. 2212738.

(7) Liu, Q.; Chen, M.; Gu, P.; Tong, L.; Wang, P.; Zhu, J.; Xu, Y.; Lu, G.; Luo, E.; Liang, J.; Fan, Y.; Zhang, X.; Sun, Y. Covalently grafted biomimetic matrix reconstructs the regenerative microenvironment of the porous gradient polycaprolactone scaffold to accelerate bone remodeling. *Small* **2023**, *19*, No. 2206960.

(8) Tang, W.; Lin, D.; Yu, Y.; Niu, H.; Guo, H.; Yuan, Y.; Liu, C. Bioinspired trimodal macro/micro/nano-porous scaffolds loading rhBMP-2 for complete regeneration of critical size bone defect. *Acta Biomater.* **2016**, *32*, 309−323.

(9) Lin, D.; Chai, Y.; Ma, Y.; Duan, B.; Yuan, Y.; Liu, C. Rapid initiation of guided bone regeneration driven by spatiotemporal delivery of IL-8 and BMP-2 from hierarchical MBG-based scaffold. *Biomaterials* **2019**, *196*, 122−137.

(10) Baino, F.; Fiorilli, S.; Brovarone, C. V. Bioactive glass-based materials with hierarchical porosity for medical applications: Review of recent advances. *Acta Biomater.* **2016**, *42*, 18−32.

(11) Arcos, D.; Vallet-Regí, M. Bioceramics for drug delivery. *Acta Mater.* **2013**, *61*, 890−911.

(12) Wu, C.; Zhang, Y.; Zhu, Y.; Friis, T.; Xiao, Y. Structure-property relationships of silk-modified mesoporous bioglass scaffolds. *Biomaterials* **2010**, *31*, 3429−3438.

(13) Zhu, Y.; Liang, H.; Liu, X.; Wu, J.; Yang, C.; Wong, T.; Kwan, K. Y. H.; Cheung, K. M. C. Regulation of macrophage polarization through surface topography design to facilitate implant-to-bone osteointegration. *Sci. Adv.* **2012**, *7*, No. eabf6654.

(14) Cockerill, I.; Su, Y.; Lee, J. H.; Berman, D.; Young, M. L.; Zheng, Y.; Zhu, D. Micro-/nano-topography on bioresorbable zinc dictates cytocompatibility, bone cell differentiation, and macrophage polarization. *Nano Lett.* **2020**, *20*, 4594−4602.

(15) Roseti, L.; Parisi, V.; Petretta, M.; Cavallo, C.; Desando, G.; Bartolotti, I. Scaffolds for bone tissue engineering: State of the art and new perspectives. *Mater. Sci. Eng., C* **2017**, *78*, 1246−1262.

(16) Kim, D. S.; Lee, J. K.; Kim, J. H.; Lee, J.; Kim, D. S.; An, S.; Park, S. B.; Kim, T. H.; Rim, J. S.; Lee, S.; Han, D. K. Advanced PLGA hybrid scaffold with a bioactive PDRN/BMP2 nanocomplex for angiogenesis and bone regeneration using human fetal MSCs. *Sci. Adv.* **2021**, *7*, No. eabj1083, DOI: 10.1126/sciadv.abj1083.

(17) Casanovaa, E. A.; Palomo, A. R.; Stahlia, L.; Arnkea, K.; Groninger, O.; Generali, M.; Neldner, Y.; Tiziani, S.; Dominguez, A. P.; Sicairos, M. G.; Gao, Z.; Appel, C. SAXS imaging reveals optimized osseointegration properties of bioengineered oriented 3D-PLGA/aCaP scaffolds in a critical size bone defect model. *Biomaterials* **2023**, *294*, No. 121989.

(18) Liu, X.; Ma, P. X. Polymeric scaffolds for bone tissue engineering. *Ann. Biomed. Eng.* **2004**, *32*, 477−486.

(19) Gentile, P.; Chiono, V.; Carmagnola, I.; Hatton, P. V. An overview of poly(lactic-co-glycolic) acid (PLGA)-based biomaterials for bone tissue engineering. *Int. J. Mol. Sci.* **2014**, *15*, 3640−3659.

(20) Groninger, O.; Hess, S.; Mohn, D.; Schneider, E.; Stark, W.; Marsmann, S.; Wolint, P.; Calcagni, M.; Cinelli, P.; Buschmann, J. Directing stem cell commitment by amorphous calcium phosphate nanoparticles incorporated in PLGA: relevance of the free calcium ion concentration. *Int. J. Mol. Sci.* **2020**, *21* (7), 2627.

(21) Gao, S.; Calcagni, M.; Welti, M.; Hemmi, S.; Hild, N.; Stark, W. J.; Burgisser, G. M.; Wanner, G. A. Proliferation of ASC-derived endothelial cells in a 3D electrospun mesh: impact of bone-biomimetic nanocomposite and co-culture with ASC-derived osteoblasts. *Injury* **2014**, *45*, 974−980.

(22) Samavedi, S.; Whittington, A. R.; Goldstein, A. S. Calcium phosphate ceramics in bone tissue engineering: a review of properties and their influence on cell behavior. *Acta Biomater.* **2013**, *9*, 8037−8045.

(23) Liu, Z.; Qu, S.; Zheng, X.; Xiong, X.; Fu, R.; Tang, K. Effect of polydopamine on the biomimetic mineralization of mussel-inspired calcium phosphate cement *in vitro*. *Mater. Sci. Eng. C* **2014**, *44*, 44−51.

(24) Du, J.; Zhou, Y.; Bao, X.; Kang, Z.; Huang, J.; Xu, G.; Yi, C.; Li, D. Surface polydopamine modification of bone defect repair materials: Characteristics and applications. *Front. Bioeng. Biotechnol.* **2022**, *10*, No. 974533.

(25) Salazar, P.; Martin, M.; González-Mora, J. Polydopamine-modified surfaces in biosensor applications. *Polym. Sci. Res. Adv.* **2016**, *7*, 385−396.

(26) Yang, W.; Zhang, X.; Wu, K.; Liu, X.; Jiao, Y.; Zhou, C. Improving cytoactive of endothelial cell by introducing fibronectin to

the surface of poly L-Lactic acid fiber mats via dopamine. *Mater. Sci. Eng., C* **2016**, *69*, 373−379.

(27) Sun, X.; Yang, J.; Ma, J.; Wang, T.; Zhao, X.; Zhu, D.; Jin, W.; Zhang, K.; Sun, X.; Shen, Y.; Xie, N. Three-dimensional bioprinted BMSCs-laden highly adhesive artificial periosteum containing gelatin-dopamine and graphene oxide nanosheets promoting bone defect repair. *Biofabrication* **2023**, *15*, No. 025010.

(28) Ma, W.; Yang, M.; Wu, D.; Li, Y.; Wang, L. S.; El-Seedi, H. R.; Wu, C.; Du, M. Fish skin gelatin-based adhesive hydrogels loading cod peptides with osteogenic activity for bone tissue engineering. *Colloid Surface A* **2023**, *673*, 13169.

(29) Qutachi, O.; Vetsch, J. R.; Gill, D.; Cox, H.; Scurr, D. J.; Hofmann, S.; Müller, R.; Quirk, R. A.; Shakesheff, K. M.; Rahman, C. V. Injectable and porous PLGA microspheres that form highly porous scaffolds at body temperature. *Acta Biomater.* **2014**, *10*, 5090−5098.

(30) Shao, C.; Zhao, R.; Jiang, S.; Yao, S.; Wu, Z.; Jin, B.; Yang, Y.; Pan, H.; Tang, R. Citrate improves collagen mineralization via interface wetting: A physicochemical understanding of biomineralization control. *Adv. Mater.* **2018**, *30*, 1704.

(31) Gan, Y.; Li, P.; Wang, L.; Mo, X.; Zhou, Q. An interpenetrating network-strengthened and toughened hydrogel that supports cell-based nucleus pulposus regeneration. *Biomaterials* **2017**, *136*, 12−28.

(32) Boskey, A. L. Mineralization of bones and teeth. *Elements* **2007**, *6*, 385−392.

(33) Fields, C.; Cassano, A.; Allen, C.; Meyer, A.; Pawlowski, K. J.; Bowlin, G. L.; Rittgers, S. E.; Szycher, M. Endothelial cell seeding of a 4-mm I.D. polyurethane vascular graft. *J. Biomater. Appl.* **2002**, *17*, 45−70.

(34) Song, P.; Li, M.; Zhang, B.; Gui, X.; Han, Y.; Wang, L.; Zhou, W.; Guo, L.; Zhang, Z.; Li, Z.; Zhou, C.; Fan, Y.; Zhang, X. DLP fabricating of precision GelMA/HAp porous composite scaffold for bone tissue engineering application. *Composites, Part B* **2022**, *244*, No. 110163.

(35) Li, M.; Song, P.; Wang, W.; Xu, Y.; Li, J.; Wu, L.; Gui, X.; Zeng, Z.; Zhou, Z.; Liu, M.; Kong, Q.; Fan, Y.; Zhang, X.; Zhou, C.; Liu, L. Preparation and characterization of biomimetic gradient multi-layer cell-laden scaffolds for osteochondral integrated repair. *J. Mater. Chem. B* **2022**, *10*, 4172−4188.

(36) Tang, P.; Song, P.; Peng, Z.; Zhang, B.; Gui, X.; Wang, Y.; Liao, X.; Chen, Z.; Zhang, Z.; Fan, Y. Chondrocyte-laden GelMA hydrogel combined with 3D printed PLA scaffolds for auricle regeneration. *Mater. Sci. Eng., C* **2021**, *130*, 12423.

(37) Fu, S.; Feng, X.; Lauke, B.; Mai, Y. Effects of particle size, particle/matrix interface adhesion and particle loading on mechanical properties of particulate-polymer composites. *Composites, Part B* **2008**, *39*, 933−961.

(38) Niiranen, H.; Pyhältö, T.; Rokkanen, P.; Kellomäki, M.; Törmälä, P. *In vitro* and *in vivo* behavior of self-reinforced bioabsorbable polymer and self-reinforced bioabsorbable polymer/bioactive glass composites. *J. Biomed. Mater. Res., Part A* **2004**, *69*, 699−708.

(39) Oyen, M. L. Mechanical characterisation of hydrogel materials. *Int. Mater. Rev.* **2014**, *59*, 44−59.

(40) Bunpetch, V.; Zhang, X. A.; Li, T.; Lin, J. X.; Maswikiti, E. P. Silicate-based bioceramic scaffolds for dual-lineage regeneration of osteochondral defect. *Biomaterials* **2019**, *192*, 323−333.

(41) Bedilu, A. A.; Amin, S. R.; Kibret, M. Hydroxyapatite formation on sol-gel derived poly(ε-caprolactone)/bioactive glass hybrid biomaterials. *ACS Appl. Mater. Interfaces* **2012**, *4*, 3148−3156.

(42) Wang, L.; Fan, L.; Zong, P.; Fuchs, J.; Sabine, L. Self-healing silk fibroin-based hydrogel for bone regeneration: dynamic metal-ligand self-assembly approach. *Adv. Funct. Mater.* **2017**, *27*, No. 1700591.

(43) Milazzo, M.; Negrini, N. C.; Scialla, S.; Marelli, B.; Buehler, M. J. Additive manufacturing approaches for hydroxyapatite-reinforced composites. *Adv. Funct. Mater.* **2019**, *29* (5), No. 1903055.

(44) Hu, X.; Zhang, P.; Chen, H.; Xie, X. GPNMB enhances bone regeneration by promoting angiogenesis and osteogenesis: Potential role for tissue engineering bone. *J. Cell. Biochem.* **2013**, *114*, 2729−2737.

(45) Zheng, C.; Wang, J.; Deng, N.; Liu, J. Functional selenium nanoparticles enhanced stem cell osteoblastic differentiation through BMP signaling pathways. *Adv. Funct. Mater.* **2014**, *24*, 6872.